MATERIALS CHEMISTRY FRONTIERS

REVIEW

View Article Online
View Journal | View Issue

Cite this: *Mater. Chem. Front.*, 2023, **7**, 5744

Nitrides: a promising class of nonlinear optical material candidates†

Xin Zhao, [ac] Chensheng Lin, [a] Haotian Tian,[ac] Chao Wang,[ac] Ning Ye[d] and Min Luo *[ab]

Received 9th June 2023,
Accepted 9th August 2023

DOI: 10.1039/d3qm00657c

rsc.li/frontiers-materials

Nonlinear optical (NLO) materials play a crucial role in all-solid-state lasers, as their frequency conversion effects enable the expansion of the limited and fixed frequency outputs of lasers to encompass both ultraviolet and infrared regions. Nitrides have emerged as highly promising NLO candidate materials, primarily due to their potentially large second-order NLO coefficients and extensive band gaps. In recent years, nitride NLO crystals have garnered significant interest from researchers, leading to the discovery of several NLO nitrides. This review provides a comprehensive overview of both reported and potential NLO nitrides, with a particular focus on their crystal structures, in order to gain a deeper understanding of the correlations between their structure and properties. Potential NLO nitrides are analyzed using density functional theory (DFT) as a basis. Additionally, this review addresses the existing challenges and offers insights into the prospective advancements in the field of NLO nitrides, fostering further discussion and exploration.

1. Introduction

Nonlinear optical (NLO) crystals have garnered significant attention due to their crucial role in advancing laser science and technology.[1–7] The conversion of laser frequency can be achieved through various up- and down-conversion processes in NLO crystals, such as second-order harmonic generation (SHG), sum frequency generation (SFG), difference frequency generation (DFG), optical parametric oscillation (OPO), and optical parametric amplification (OPA).[8] Over the past few decades, several promising deep-ultraviolet (DUV), ultraviolet-visible (UV-Vis), and infrared (IR) crystals have been discovered and extensively researched, such as $KBe_2BO_3F_2$ (KBBF),[9] LiB_3O_5 (LBO),[10] β-BaB_2O_4 (β-BBO),[11] KH_2PO_4 (KDP),[12] $KTiOPO_4$ (KTP),[13] $AgGaS_2$(AGS),[14] $AgGaSe_2$(AGSe)[15] and $ZnGeP_2$(ZGP).[16] In general, an outstanding NLO crystal should exhibit a comprehensive set of performance characteristics, including: (i) a strong second-order harmonic generation (SHG) response, (ii) a high laser damage threshold (LDT) inherently related to wide band gaps (E_g) of materials, (iii) a wide optical transparency range, (iv) appropriate birefringence (Δn) for achieving the phase-matching behavior, and (v) favourable physical and chemical properties.

Over the past decades, the exploration of inorganic NLO crystals in the DUV and UV-Vis regions has mainly focused on borates, carbonates, nitrates, phosphates and sulfates.[17–22] Borates have been extensively synthesized and reported as UV and DUV NLO crystals due to their remarkable structural diversity, which combines various structural motifs such as BO_3^{3-}, BO_4^{5-}, $B_2O_5^{4-}$, $B_3O_6^{3-}$ and $B_3O_7^{5-}$ anionic groups, resulting in exceptional properties. Carbonates and nitrates have exhibited significant SHG responses and birefringence, attributed to their π-conjugated planar triangles. Phosphates and sulfates, on the other hand, possess broad band gaps and optical transparency, but their hyperpolarizabilities and optical anisotropy are weaker. As regarding the study of IR NLO materials, inorganic chalcogenides,[23] halides,[24] and pnictides[25,26] have been widely acknowledged as promising systems for IR NLO materials. Among these, chalcogenides have received the most attention due to their comprehensive NLO properties. Generally, halides exhibit excellent IR transparency and large band gaps resulting in high laser damage threshold (LDT). However, their SHG coefficients are typically much smaller compared to chalcogenides and pnictides. In contrast, pnictides tend to have larger effective nonlinear coefficients (d_{eff}) but smaller band gaps ($E_g < 2.5$ eV) when compared to chalcogenides and halides.

Nitrides are considered multifunctional materials with widespread applications in various fields, such as semiconductors, catalysis, energy storage, and spintronics.[27–29] In fact, nitrides

[a] *Key Laboratory of Optoelectronic Materials Chemistry and Physics, Fujian Institute of Research on the Structure of Matter, Chinese Academy of Sciences, Fuzhou, Fujian 350002, China. E-mail: lm8901@fjirsm.ac.cn*
[b] *Fujian Science & Technology Innovation Laboratory for Optoelectronic Information of China, Fuzhou, Fujian 350108, China*
[c] *University of Chinese Academy of Sciences, Beijing 100049, China*
[d] *Tianjin Key Laboratory of Functional Crystal Materials, Institute of Functional Crystal, Tianjin University of Technology, Tianjin 300384, China*

† Electronic supplementary information (ESI) available: The method of theoretical calculation, band structure (HSE06), PDOS, calculated frequency-dependent coefficients and calculated refractive index dispersion curves of compounds. See DOI: https://doi.org/10.1039/d3qm00657c

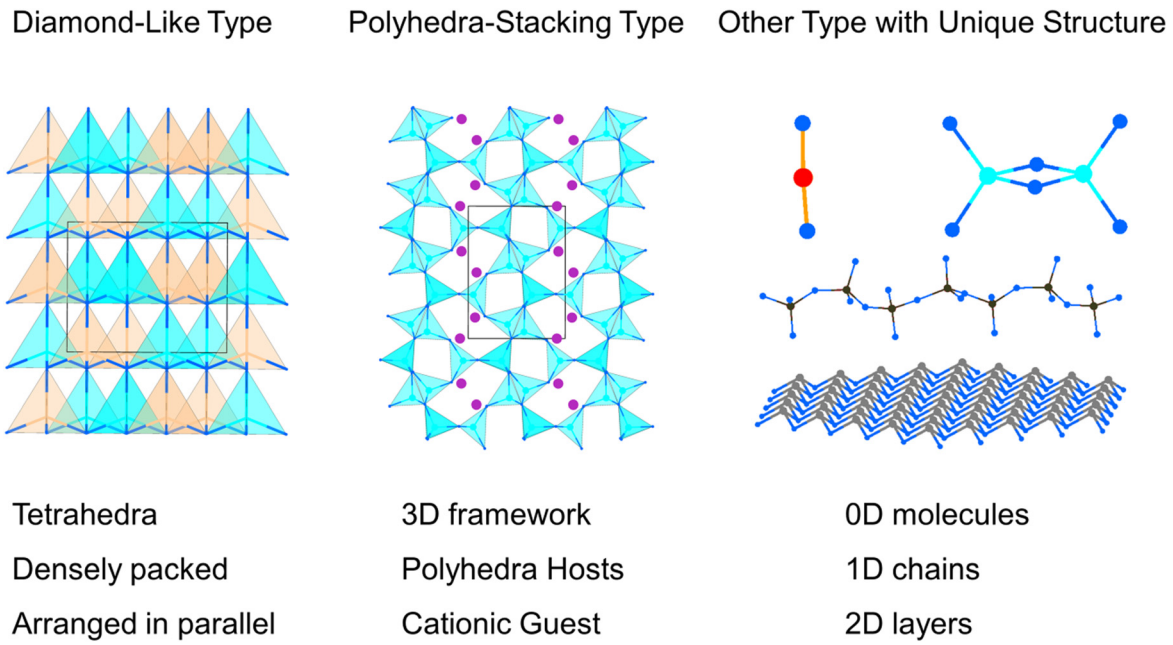

Fig. 1 Schematic representation of the three categories of NLO nitrides according to structural features.

hold great potential as a system for developing NLO crystals, owing to their several advantages: (i) a wide band gap and high thermal conductivity, which contribute to a high LDT in crystals; (ii) excellent thermal stability; (iii) broad transparency windows ranging from the UV to mid-IR region. Consequently, nitrides have garnered significant interest among researchers, and several nitrides have been investigated as NLO materials through experimental approaches and computational tools, such as Zn_2NX (X = Cl, Br), $MoZn_3N_4$, $TiZnN_2$ and $AGeN_2$ (A = Sr, Ba).[30–33] However, NLO nitrides with outstanding properties remain scarce, and the structure–property relationships in NLO nitrides have not been thoroughly explored. Therefore, a comprehensive study of the characteristics and structure–property correlations in NLO nitrides is urgently needed. In this work, we summarize and categorize recently reported and potential NLO nitrides into three groups based on their structural features: (i) 19 diamond-like (DL) type NLO nitrides; (ii) 19 polyhedra-stacking type NLO nitrides; and (iii) 7 other NLO nitrides with distinctive structures, the structural features of the three categories of NLO nitrides are illustrated in Fig. 1. A detailed analysis of these compounds' crystal structures, NLO properties, and structure–property correlations was provided. Furthermore, the current challenges and future directions for the development of NLO nitrides were discussed.

2. Diamond-like type NLO nitrides

Diamond-like (DL) structures represent a rich source of non-centrosymmetric (NCS) structures found in nature. These DL compounds have garnered significant interest as potential mid-IR NLO candidates due to several key advantages: (i) their intrinsic NCS crystal structures and diverse building motifs, which are formed by MQ_4 (M = Si, Ge, Sn, Ga, In, Zn, Cd, Hg, Cu, Ag and Li; Q = S, Se, N and P) tetrahedra, (ii) their broad IR transparency range, which is attributed to the covalent M–Q bonds; and (iii) the fundamental building blocks of $[MQ_4]$ tetrahedra in DL structures, which are consistently interconnected through an aligned arrangement.[34] This alignment is anticipated to lead to an additive superposition of the microscopic second-order susceptibility, thereby facilitating a strong SHG response. As a result, numerous DL metal chalcogenides and pnictides with exceptional NLO performance have been reported, such as $Li_4MgGe_2S_7$, $HgCuPS_4$, Li_2ZnGeS_4, $MnSiP_2$, $M^{II}_3P_nI_3$ (M^{II} = Zn and Cd, P_n = P and As) and $Mg_2In_3Si_2P_7$.[35–40] DL nitrides, when employed as NLO materials, may offer the following benefits: (i) large NLO coefficients ascribed to the parallel alignment of $[MN_4]$ tetrahedra; (ii) wide band gaps and high thermal conductivity, which contribute to a significant LDT; and (iii) stable physical and chemical properties.

2.1. GaN and AlN

Group-III nitrides are promising materials for various technological applications, such as short-wavelength light-emitting diodes, semiconductor lasers, and optical detectors.[41] The linear and nonlinear optical properties of GaN and AlN have been both theoretically and experimentally studied in the past decades.[42,43] GaN and AlN crystalized in the hexagonal crystal system with space group of $P6_3mc$, and the structure of AlN was shown in Fig. 2a. The $[AlN_4]$ tetrahedra were interconnected by sharing corners and aligned along the *c*-axis. The experimental optical band gaps of GaN and AlN were 3.50 and 6.20 eV,[44,45] respectively, and their band gaps between valence bands and conduction bands are mainly dominated by the covalent Al–N and Ga–N bands (Fig. S9a and b, ESI†). As listed in Table 1, the calculated NLO coefficients were d_{31} = 2.42, d_{33} = −3.64 pm V^{-1}

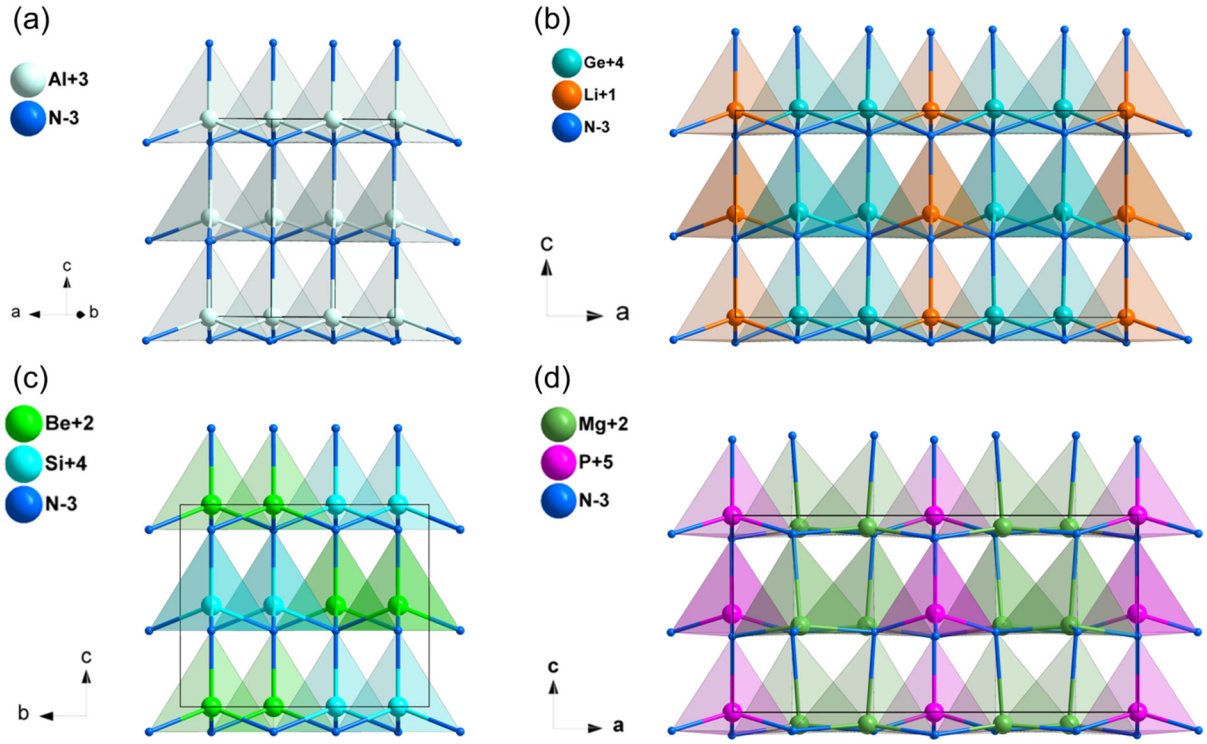

Fig. 2 Crystal structure of AlN (a), $LiGe_2N_3$ (b), $BeSiN_2$ (c) and Mg_2PN_3 (f).

Table 1 The NLO data of diamond-like type Nitrides

Compounds	Space group	Band gap (eV)			NLO coefficients[a] (pm V^{-1})	Δn[a]	
		GGA[a]	HSE06[a]	Exp.[b]		At 1064 nm	At 2050 nm
GaN	$P6_3mc$	1.93	2.87	3.5	d_{31} = 2.42, d_{33} = −3.64	0.017	0.015
AlN	$P6_3mc$	3.86	5.12	6.2	d_{31} = 0.23, d_{33} = 0.86	0.023	0.022
$LiSi_2N_3$	$Cmc2_1$	5.16	6.45	6.4	d_{31} = 1.01, d_{32} = 0.24, d_{33} = −0.32	0.043	0.042
$LiGe_2N_3$	$Cmc2_1$	1.45	2.57	3.9	d_{31} = 4.14, d_{32} = 5.30, d_{33} = −2.60	0.071	0.069
$BeSiN_2$	$Pna2_1$	5.22	6.53	—	d_{31} = 0.74, d_{32} = 0.91, d_{33} = 0.45	0.031	0.030
$MgSiN_2$	$Pna2_1$	4.18	5.49	4.8	d_{31} = 0.52, d_{32} = 1.86, d_{33} = 0.32	0.017	0.017
$MgGeN_2$	$Pna2_1$	2.21	3.35	3.2	d_{31} = 6.05, d_{32} = 5.59, d_{33} = −12	0.032	0.033
$ZnSiN_2$	$Pna2_1$	3.41	4.58	3.7	d_{31} = −3.01, d_{32} = −6.05, d_{33} = 7.61	0.051	0.049
$ZnGeN_2$	$Pna2_1$	2.01	3.01	3.2	d_{31} = −4.82, d_{32} = −5.2, d_{33} = 8.13	0.039	0.038
Zn_3MoN_4	$Pmn2_1$	1.91	2.77	2.4	d_{31} = 13.4, d_{32} = 14.57	0.098	0.088
Mg_2PN_3	$Cmc2_1$	3.20	4.43	5.0	d_{31} = 1.99, d_{32} = 2.73, d_{33} = −2.33	0.072	0.071
Zn_2PN_3	$Cmc2_1$	2.83	4.00	3.7	d_{31} = 4.43, d_{32} = 6.70, d_{33} = −9.03	0.003	0.003
Mg_2SbN_3	$Cmc2_1$	1.45	2.51	—	d_{31} = 0.26, d_{32} = 1.50, d_{33} = 3.47	0.031	0.027
$LiPN_2$	$I\bar{4}2d$	3.93	5.21	—	d_{14} = d_{36} = 0.20	0.022	0.016
$CuPN_2$	$I\bar{4}2d$	2.12	3.19	—	d_{14} = d_{36} = −8.26	0.019	0.018
Zn_2NCl	$Pna2_1$	2.25	3.31	3.21	d_{31} = 5.14, d_{32} = 7.30, d_{33} = 12.89	0.065	0.062[b]
Zn_2NBr	$Pna2_1$	2.38	3.09	2.28	d_{31} = 4.51, d_{32} = 6.35, d_{33} = 11.15	0.071	0.069[b]
LiSiON	$Pca2_1$	5.48	7.03	—	d_{31} = 1.33, d_{32} = −2.40, d_{33} = −0.14	0.044	0.043
Li_2P_2ON	$Cmc2_1$	5.21	6.82	—	d_{31} = 0.18, d_{32} = 0.33, d_{33} = 0.75	0.045	0.044

[a] This work. [b] Other work from ref. 27, 41, 42, 44, 45, 48, 49, 53.

for GaN, and d_{31} = 0.23, d_{33} = 0.86 pm V^{-1} for AlN, and the calculated birefringence is 0.017 for GaN and 0.023 for AlN at 1064 nm.

2.2. $LiSi_2N_3$ and $LiGe_2N_3$

Both $LiSi_2N_3$[46] and $LiGe_2N_3$[47] crystalized in the space group of $Cmc2_1$. Taking $LiGe_2N_3$ as an example, the $[LiN_4]$ tetrahedra and $[GeN_4]$ tetrahedra connected through sharing N atoms, the $[LiN_4]$ and $[GeN_4]$ tetrahedra in $LiGe_2N_3$ are perfectly aligned parallel to the *c*-axis (Fig. 2b). However, $[SiN_4]$ tetrahedra in $LiSi_2N_3$ are at an acute angle to the *c*-axis (Fig. S1a, ESI†). As shown in Table 1, the experimental band gaps of $LiSi_2N_3$ and $LiGe_2N_3$ are 6.40 and 3.90 eV,[48] and their band gaps between valence bands and conduction bands are mainly dominated by the covalent Si–N and Ge–N bands (Fig. S9c and d, ESI†). The calculated NLO coefficients were d_{31} = 1.01, d_{32} = 0.24,

d_{33} = −0.32 pm V^{-1} for $LiSi_2N_3$, and d_{31} = 4.14, d_{32} = 5.3, d_{33} = −2.60 pm V^{-1} for $LiGe_2N_3$. Additionally, their calculated birefringence is about 0.043 ($LiSi_2N_3$) and 0.071 ($LiGe_2N_3$) at 1064 nm.

2.3. A–M^{IV}–N_2 (A = Be, Mg, Zn; M^{IV} = Si, Ge) system

$BeSiN_2$,[49] $MgSiN_2$, $MgGeN_2$,[50] $ZnSiN_2$ and $ZnGeN_2$[51] are isostructural and their space group is $Pna2_1$, thus $BeSiN_2$ was chosen for the analysis of their structural features. Both [BeN_4] and [SiN_4] tetrahedra in $BeSiN_2$ are arranged along the same direction and connected by sharing corners (Fig. 2c). The calculated band gap of $BeSiN_2$ is 6.53 eV (HSE06), and the experimental band gaps are 4.80, 3.20, 3.70 and 3.20 eV for $MgSiN_2$, $MgGeN_2$, $ZnSiN_2$ and $ZnGeN_2$, respectively. Their band gaps between valence bands and conduction bands are mainly dominated by the covalent A–N and M^{IV}–N bands (Fig. S9e, f and S10a–c, ESI†). In addition, the calculated NLO coefficients and birefringence of A–M^{IV}–N_2 (A = Be, Mg, Zn; M^{IV} = Si, Ge) system were listed in Table 1. The results show that $MgGeN_2$ (E_g = 3.2 eV, d_{33} = −12 pm V^{-1}) exhibits balanced NLO properties.

2.4. Zn_3MoN_4

The compound Zn_3MoN_4[52] crystallizes the space group of $Pmn2_1$ and its structure is displayed in Fig. 3a. The crystal structure of Zn_3MoN_4 is formed by stacking [ZnN_4] and [MoN_4] tetrahedra along the *c*-axis, and these tetrahedra are connected by sharing tetrahedral vertices. As shown in Table 1, the calculated band gap by HSE06 is 2.77 eV for Zn_3MoN_4, and the band gap between valence bands and conduction bands is mainly dominated by the covalent Mo–N bands (Fig. S10d, ESI†). Moreover, the calculated NLO coefficients are d_{31} = 13.4, d_{32} = 14.57 and d_{33} = −26.04 pm V^{-1}, and the d_{33} coefficient is about 1.7 times that of AGS (15.3 pm V^{-1}). According to the results, its calculated birefringence is about 0.098 at 1064 nm, illustrating that Zn_3MoN_4 could achieve phase-matching behavior in the IR NLO application.

2.5. A–M–N (A = Li, Cu, Mg, Zn; M = P, Sb) system

Mg_2PN_3, Zn_2PN_3 and $MgSbN_3$. Mg_2PN_3,[53] Zn_2PN_3[54] and $MgSbN_3$[55] crystalized in the same space group $Cmc2_1$. Taking Mg_2PN_3 as an example, its crystal structure featured densely packed layers consisting of [MgN_4] and [PN_4] tetrahedra, which were all oriented towards the *c*-axis (Fig. 2d). The experimental band gaps were 5.0 and 3.7 eV for Mg_2PN_3 and Zn_2PN_3,[56] and the calculated band gap of $MgSbN_3$ was 2.51 eV (HSE06). The band gaps of Mg_2PN_3 and $MgSbN_3$ between valence bands and conduction bands are mainly dominated by the covalent Mg–N, P–N and Sb–N bands, while the band gap of Zn_2PN_3 is mainly contributed by Zn–N bonds (Fig. S10e, f and S11a, ESI†). Furthermore, the calculated NLO coefficients are d_{31} = 1.99, d_{32} = 2.73, d_{33} = −2.33 pm V^{-1} for Mg_2PN_3, d_{31} = 4.43, d_{32} = 6.70, d_{33} = −9.03 pm V^{-1} for Zn_2PN_3, and d_{31} = 0.26, d_{32} = 1.50, d_{33} = 3.47 pm V^{-1} for $MgSbN_3$, respectively. In addition, the calculated birefringence of Mg_2PN_3, Zn_2PN_3 and $MgSbN_3$ is 0.072, 0.003 and 0.031 at 1064 nm, respectively (Table 1).

$LiPN_2$ and $CuPN_2$. $LiPN_2$[57] and $CuPN_2$[58] are isostructural with the space group of $I\bar{4}2d$. $LiPN_2$ was chosen as an example

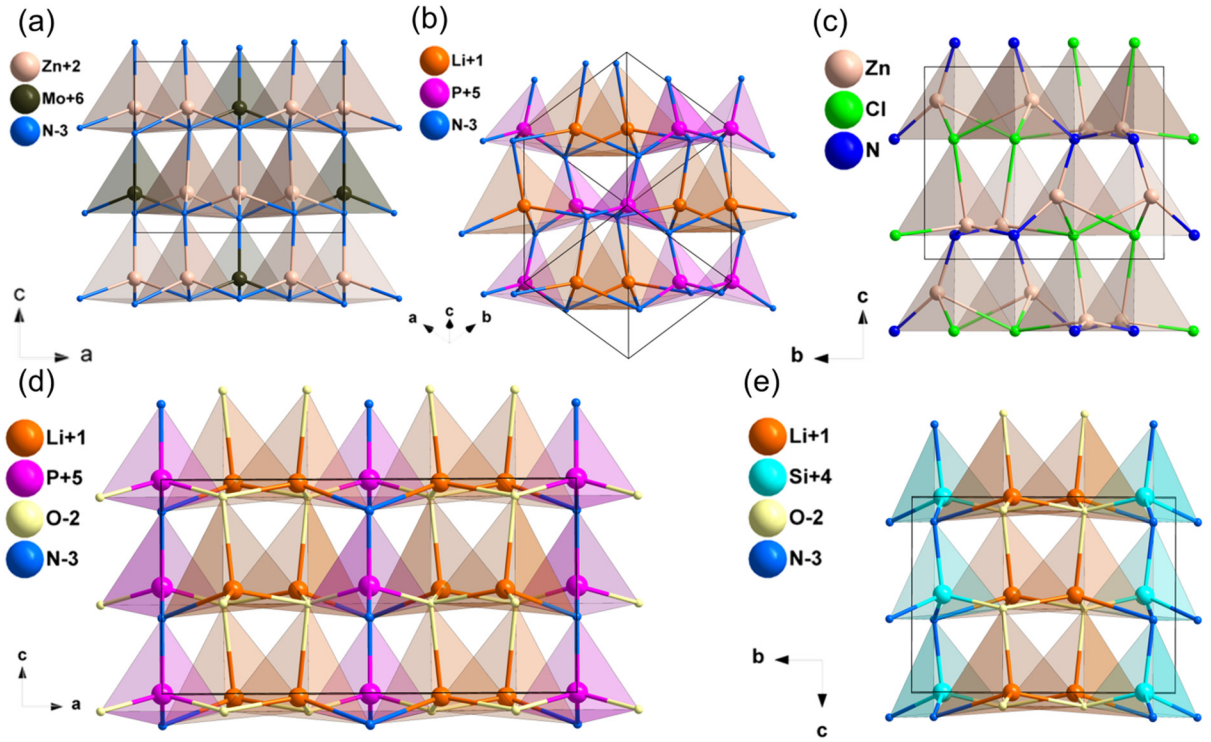

Fig. 3 Crystal structure of Zn_3MoN_4 (a), $LiPN_2$ (b), Zn_2NCl (c), Li_2PO_2N (d) and LiSiON (e).

to describe the structure (Fig. 3b), which was composed of $[LiN_4]$ and $[PN_4]$ tetrahedra, and they were arranged in nearly the same direction. As shown in Table 1, the HSE06 band gaps of $LiPN_2$ and $CuPN_2$ were 5.21 and 3.19 eV, respectively, which were larger than $LiGaS_2$ (3.62 eV), and their band gaps between valence bands and conduction bands are mainly dominated by the Li–N, Cu–N and P–N bands (Fig. S11b and c, ESI†). The NLO coefficients of $LiPN_2$ and $CuPN_2$ were calculated to be $d_{14} = d_{36} = 0.20$ pm V^{-1} ($LiPN_2$) and $d_{14} = d_{36} = -8.26$ pm V^{-1} ($CuPN_2$), and their calculated birefringence is 0.022 and 0.019 at 1064 nm, respectively.

2.6. Diamond-like nitrides with mixed anions

Zn_2NX (X = Cl, Br). Zn_2NX (X = Cl, Br) were synthesized and reported as mid-IR NLO materials in 2021 by our group.[30] These two compounds are isostructural and crystallize in space group $Pna2_1$. In the structure of Zn_2NCl, the distorted $[ZnN_2Cl_2]$ tetrahedra are connected to each other *via* sharing N and Cl atoms and stacked along the same direction (Fig. 3c). The two compounds exhibit excellent mid-IR NLO performances. The experimental band gaps are 3.21 and 3.28 eV for Zn_2NCl and Zn_2NBr, both of which are larger than 3.00 eV. The two compounds exhibit large SHG responses which are 0.9 and 0.8 times that of AGS at 2050 nm, respectively. They also have high LDTs of 20.7 and 25.9 times that of AGS respectively. All the mentioned above mid-IR NLO properties are listed in Table 1. These results showed that Zn_2NX (X = Cl, Br) are potential candidates as good IR NLO materials.

LiSiON. LiSiON[59] crystallizes in space group $Pca2_1$ and its crystal structure is displayed in Fig. 3e. The $[SiN_3O]$ and $[LiNO_3]$ tetrahedra with mixed anions were interconnected *via* sharing the N and O atoms, which were aligned in nearly the same direction. The calculated results of LiSiON are given in Table 1, the HSE06 band gap is 7.03 eV, which is mainly dominated by the covalent Si–O and Si–N bands (Fig. S11d, ESI†). LiSiON has three independent non-vanishing NLO tensor components (d_{31}, d_{32}, d_{33}), and the calculated value are $d_{31} = 1.33$, $d_{32} = -2.40$ and $d_{33} = -0.14$ pm V^{-1}. LiSiON exhibits a large birefringence with the calculated value of 0.044 at 1064 nm.

Li_2PO_2N. The compound Li_2PO_2N[60] crystallizes in space group $Cmc2_1$. In the structure of Li_2PO_2N, $[PN_2O_2]$ tetrahedra are stacked parallel to the *c*-axis, and $[LiNO_3]$ tetrahedra are at an acute angle to the *c*-axis, both of which are connected by sharing N and O atoms (Fig. 3d). The HSE06 band gap of Li_2PO_2N is 6.82 eV, which is mainly dominated by the covalent P–O and P–N bands (Fig. S11e, ESI†). The calculated NLO coefficients are $d_{31} = 0.18$, $d_{32} = 0.33$ and $d_{33} = 0.75$ pm V^{-1}. Notably, the computational birefringence of Li_2PO_2N is 0.045 at 1064 nm (Table 1).

3. Polyhedra-stacking type NLO nitrides

The design of polyhedra-stacking type compounds serves as a prevalent and effective approach for discovering exceptional NLO crystals. These compounds are characterized by a three-dimensional (3D) framework formed through the combination of $[MQ_4]$ (M = Ag, Cd, Ga, P, S,Ge, *etc.* Q = P, O, S and Se) with highly electropositive alkali earth elements (Li, Na, K, Rb, Cs) and alkali metals (Mg, Ca, Sr, Ba), or rare earth elements (La, Sc, Y, Lu) possessing a full shell. Polyhedra-stacking type NLO nitrides offer two primary advantages. Firstly, the structural frameworks of these compounds exhibit a wide variety, presenting opportunities for the development of innovative structures. Secondly, the structure of these compounds possesses the potential for rational adjustment, allowing for the achievement of a balance between a robust SHG response and a broad bandgap. This can be accomplished by modifying the cations to enable parallel alignment of the $[MQ_4]$ tetrahedra.

3.1. Alkali metal-based polyhedra-stacking type NLO nitrides

$NaSi_2N_3$ and $NaGe_2N_3$. $NaSi_2N_3$[61] and $NaGe_2N_3$[62] are isostructural and their space group is $Cmc2_1$. In their structure, the adjacent $[Si/GeN_4]$ tetrahedra connected by sharing N atoms to form a layer in *b–c* plane, the structural framework made up by connecting layers and Na^+ filled in the holes (Fig. 4). The calculated band gaps by HSE06 are 5.31 eV for $NaSi_2N_3$ and 4.17 eV for $NaGe_2N_3$, which are mainly dominated by the covalent Si/Ge–N bonds and ionic Na–N interactions (Fig. S12a and b, ESI†). The calculated NLO coefficients are $d_{31} = 0.33$, $d_{32} = 0.73$, $d_{33} = -0.65$ pm V^{-1} for $NaSi_2N_3$ and $d_{31} = 4.74$, $d_{32} = 1.59$, $d_{33} = -4.36$ pm V^{-1}, respectively. In addition, their calculated birefringence is 0.064 and 0.048 at 1064 nm, respectively. All the above results are listed in Table 2.

$NaPN_2$. $NaPN_2$[63,64] crystallizes in the tetragonal space group $I\bar{4}2d$. In this structure, $[PN_4]$ tetrahedra attached by sharing corners and expanded in the space to form the structural framework, while Na^+ filled in the intervals to balance the residual charge (Fig. 5a). As listed in Table 2, the calculated band gap of $NaPN_2$ is 6.16 eV (HSE06), which is mainly dominated by the covalent P–N bonds and ionic Na–N interactions (Fig. S11f, ESI†). The calculated NLO coefficient is $d_{14} = d_{36} = -1.97$ pm V^{-1}, and the birefringence of $NaPN_2$ was calculated to be 0.042 at 1064 nm.

3.2. Alkaline earth metals-based polyhedra-stacking type NLO nitrides

$CaGeN_2$. $CaGeN_2$[65] crystallizes in tetragonal space group $I\bar{4}2d$. In the structural framework of $CaGeN_2$, $[GeN_4]$ tetrahedra interconnected by vertex-sharing and arranged along the same direction (Fig. 5d). $CaGeN_2$ has a wider HSE06 band gap of 4.31 eV compared to $ZnGeN_2$ (3.01 eV), which is mainly dominated by the covalent Ge–N bonds (Fig. S12c, ESI†). The calculated NLO coefficient d_{14} and birefringence are -5.74 pm V^{-1} and 0.060 at 1064 nm, respectively (Table 2).

CaP_2N_4 and SrP_2N_4. CaP_2N_4[66] and SrP_2N_4[67] are isostructural and they crystallized in the polar space group $P6_3$. Taking CaP_2N_4 as an example, the $[PN_4]$ tetrahedra stacked according to the symmetry of 6_3 screw axis and connected *via* vertex-sharing, while Ca^{2+} are added into the holes to balance the framework (Fig. 5c, e and f). Their computational band gaps are

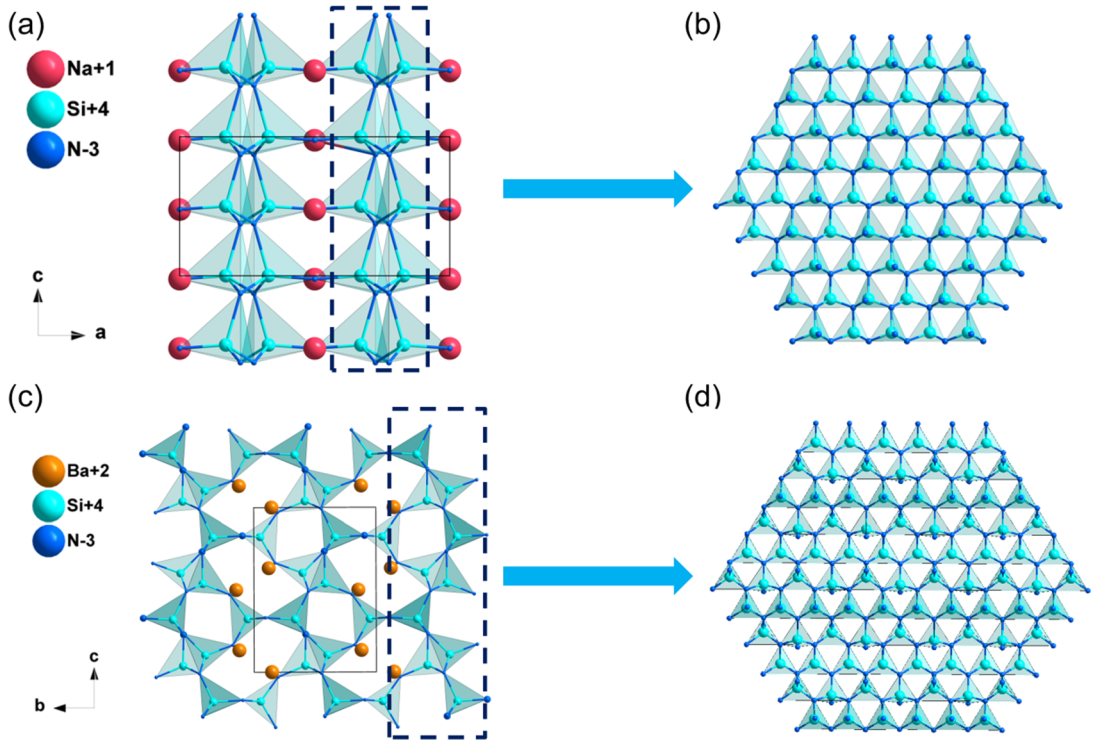

Fig. 4 Crystal structure of $NaSi_2N_3$ (a) and (b) and $Ba_2Si_5N_8$ (c) and (d).

Table 2 The NLO data of polyhedra-stacking type nitrides

Compounds	Space group	Band gap (eV)			NLO coefficients[a] (pm V^{-1})	Δn^a	
		GGA[a]	HSE06[a]	Exp.[b]		At 1064 nm	At 2050 nm
$NaSi_2N_3$	$Cmc2_1$	4.02	5.31	—	d_{31} = 0.33, d_{32} = 0.73, d_{33} = −0.65	0.064	0.063
$NaGe_2N_3$	$Cmc2_1$	2.88	4.17	—	d_{31} = 4.74, d_{32} = 1.59, d_{33} = −4.36	0.048	0.047
$NaPN_2$	$I\bar{4}2d$	4.77	6.16	—	d_{14} = d_{36} = −1.9	0.042	0.042
$CaGeN_2$	$I\bar{4}2d$	3.16	4.31	—	d_{14} = d_{36} = −5.7	0.060	0.061
CaP_2N_4	$P6_3$	4.37	5.77	—	d_{31} = −0.02, d_{33} = 0.58	0.008	0.007
SrP_2N_4	$P6_3$	3.35	4.59	—	d_{31} = 0.29, d_{33} = 0.94	0.014	0.013
$Sr_2Si_5N_8$	$Pmn2_1$	3.25	4.45	—	d_{31} = 1.01, d_{32} = 0.24, d_{33} = −0.32	0.023	0.023
$Ba_2Si_5N_8$	$Pmn2_1$	2.92	4.03	—	d_{31} = 1.01, d_{32} = 0.24, d_{33} = −0.32	0.024	0.023
$SrSi_7N_{10}$	Pc	4.05	5.27	—	d_{11} = −0.22, d_{12} = 0.57, d_{13} = 3.44 d_{31} = −0.49, d_{32} = 4.21, d_{33} = 0.44	0.018	0.018
$BaSi_7N_{10}$	Pc	3.93	5.17	—	d_{11} = −0.23, d_{12} = 0.57, d_{13} = −4.64 d_{31} = −0.52, d_{32} = −3.77, d_{33} = 0.41	0.011	0.011
$SrSi_6N_8$	$Imm2$	3.21	4.46	—	d_{31} = −1.18, d_{32} = −0.30, d_{33} = 3.82	0.043	0.042
α-$Ca_2Si_5N_8$	Cc	3.47	4.72	—	d_{11} = −0.23, d_{12} = 0.21, d_{13} = −0.08 d_{31} = −0.10, d_{32} = −0.47, d_{33} = 0.05	0.009	0.009
β-$Ca_2Si_5N_8$	$P2_1$	2.65	3.74	—	d_{14} = 0.35, d_{21} = −1.90, d_{22} = −0.71, d_{23} = −3.04	0.016	0.015
$Ca_3Al_2N_4$	$P2_12_12_1$	2.26	3.29	—	d_{14} = −0.28	0.031	0.029
$SrAlSi_4N_7$	$Pna2_1$	2.83	4.04	—	d_{31} = −1.02, d_{32} = 1.43, d_{33} = −1.34	0.028	0.027
$SrYSi_4N_7$	$P6_3mc$	2.98	4.21	3.3–3.5	d_{31} = −1.25, d_{33} = 6.45	0.012	0.011
CrB_4O_5N	$P6_3mc$	1.96[b]	—	—	0.8 × SiO_2[b]	—	—
$LaSi_3N_5$	$P2_12_12_1$	3.38	4.53	—	d_{14} = 2.50	0.037	0.036
$Pb_2Si_5N_8$	$Pmn2_1$	2.18	3.17	—	d_{31} = 6.46, d_{32} = −3.71, d_{33} = −11.84	0.064	0.042

[a] This work. [b] Other work from ref. 74, 76.

5.77 and 4.59 eV (HSE06), respectively, which are mainly dominated by the covalent P–N bonds (Fig. S12d and e, ESI†). The calculated NLO coefficients are d_{31} = −0.02, d_{33} = 0.58 pm V^{-1} for CaP_2N_4 and d_{31} = 0.29, d_{33} = 0.94 pm V^{-1} for SrP_2N_4 (Table 2), respectively. In addition, the calculated birefringence of CaP_2N_4 and SrP_2N_4 is 0.008 and 0.014 at 1064 nm.

$Sr_2Si_5N_8$ and $Ba_2Si_5N_8$. $Sr_2Si_5N_8$ and $Ba_2Si_5N_8$[68] are isostructural and crystallized in the orthorhombic space group $Pmn2_1$. In their structure, [SiN_4] tetrahedra interconnected *via* corners sharing to form interlayers in *a*–*c* plane, which consist of the structural framework through [SiN_4] tetrahedra, and Sr^{2+}/Ba^{2+} are accessed to empty positions to balance the framework

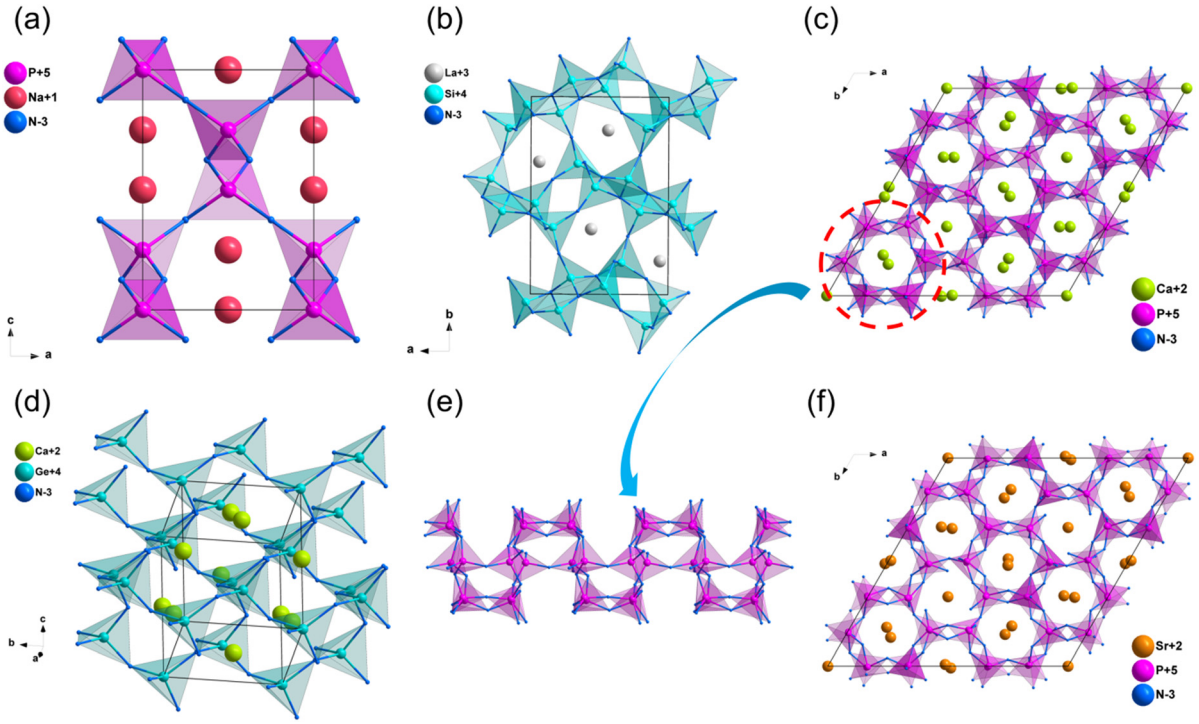

Fig. 5 Crystal structure of $NaPN_2$ (a), $LaSi_3N_5$ (b), CaP_2N_4 (c) and (e), SrP_2N_4 (f) and $CaGeN_2$ (d).

(Fig. 4c and d). The optical properties of $Sr_2Si_5N_8$ and $Ba_2Si_5N_8$ were calculated and listed in Table 2, the calculated band gaps are 4.45 eV for $Sr_2Si_5N_8$ and 4.03 eV for $Ba_2Si_5N_8$ (HSE06), which are mainly dominated by the covalent Si–N bonds (Fig. S12f and S13a, ESI†). The calculated NLO coefficients are d_{31} = 1.7, d_{32} = 1.73, d_{33} = 0.76 pm V^{-1} for $Sr_2Si_5N_8$ and d_{31} = −1.22, d_{32} = −0.91, d_{33} = −0.4 pm V^{-1} for $Ba_2Si_5N_8$. In addition, the calculated birefringence are 0.023 ($Sr_2Si_5N_8$) and 0.024 ($Ba_2Si_5N_8$) at 1064 nm, respectively.

$SrSi_7N_{10}$ and $BaSi_7N_{10}$. $SrSi_7N_{10}$[69] and $BaSi_7N_{10}$[70] are isostructural and their space group is *Pc*. In their structure, the structural framework is formed by layers (in *a*–*c* plane) and chains (parallel to *c*-axis) with Sr^{2+}/Ba^{2+} filled in the holes, where the layers are made up of corner-shared [SiN_4] tetrahedra as well as the chains constructed of corner- and prism-shared [SiN_4] tetrahedra (Fig. 6a and b). The calculated band gaps of $SrSi_7N_{10}$ and $BaSi_7N_{10}$ are 5.27 and 5.17 eV, respectively, which are mainly dominated by the covalent Si–N bonds (Fig. S13b and c, ESI†). Moreover, the calculated NLO coefficients are d_{11} = −0.22, d_{12} = 0.57, d_{13} = 3.44, d_{31} = −0.49, d_{32} = 4.21, d_{33} = 0.44 pm V^{-1} for $SrSi_7N_{10}$ and d_{11} = −0.23, d_{12} = 0.57, d_{13} = −4.64, d_{31} = −0.52 pm V^{-1}, d_{32} = −3.77, d_{33} = 0.41 pm V^{-1} for $BaSi_7N_{10}$. The calculated birefringence of $SrSi_7N_{10}$ and $BaSi_7N_{10}$ is 0.018 and 0.011 at 1064 nm, respectively.

$SrSi_6N_8$. The synthesis and crystal structure of $SrSi_6N_8$[71] were first reported in 2005 by Schnick *et al.* $SrSi_6N_8$ crystallize in the orthorhombic space group *Imm*2. As described in Fig. 6, the structural framework is constructed by [SiN_4] tetrahedra and [N_3Si–SiN_3] entities, which are bridged through N atoms with Sr^{2+} distributed in the holes. Interestingly, [N_3Si–SiN_3] entities contain additional Si–Si single bonds, which might enhance the SHG performance of $SrSi_6N_8$. The HSE06 band gap of $SrSi_6N_8$ is 4.46 eV, and the band gap between valence bands and conduction bands is mainly dominated by the covalent Si–N bonds (Fig. S13d, ESI†). The calculated NLO coefficient are d_{31} = −1.18, d_{32} = −0.3, d_{33} = 3.82 pm V^{-1}. Notably, the computational birefringence of $SrSi_6N_8$ is 0.043 at 1064 nm (Table 2).

α-$Ca_2Si_5N_8$ and β-$Ca_2Si_5N_8$. α-$Ca_2Si_5N_8$[72,73] and β-$Ca_2Si_5N_8$[74] are isomers, where the former crystallizes in the monoclinic space group *Cc* and the latter crystallizes in the monoclinic space group $P2_1$. As can be seen in Fig. 7, both α-$Ca_2Si_5N_8$ and β-$Ca_2Si_5N_8$ have a structural framework similar to $Ba_2Si_5N_8$, including layers made up of [SiN_4] tetrahedra and the ways they connected. The HSE06 band gaps are 4.72 and 3.74 eV for α-$Ca_2Si_5N_8$ and β-$Ca_2Si_5N_8$, respectively, which are mainly dominated by the covalent Si–N bonds (Fig. S13e and f, ESI†). The calculated NLO coefficients are d_{11} = −0.23, d_{12} = 0.21, d_{13} = −0.08, d_{31} = 0.1, d_{32} = −0.47, d_{33} = 0.05 pm V^{-1} for α-$Ca_2Si_5N_8$ and d_{21} = −1.99, d_{22} = −0.71, d_{23} = −3.04, d_{14} = 0.35 pm V^{-1} for β-$Ca_2Si_5N_8$. Furthermore, the calculated birefringence of α-$Ca_2Si_5N_8$ and β-$Ca_2Si_5N_8$ is 0.009 and 0.016 at 1064 nm.

$Ca_3Al_2N_4$. The compound $Ca_3Al_2N_4$[75] crystallizes in orthorhombic space group $P2_12_12_1$. In the structure, [AlN_4] tetrahedra are connected by sharing corners and prisms to form chains, which extend into the space to constitute the framework with Ca^{2+} dispersed in the intervals to stabilize the structure (Fig. 8a and b). The calculated band gap of $Ca_3Al_2N_4$ is 3.29 eV (HSE06), which is mainly dominated by the covalent Al–N bonds and ionic Ca–N interactions (Fig. S14a, ESI†).

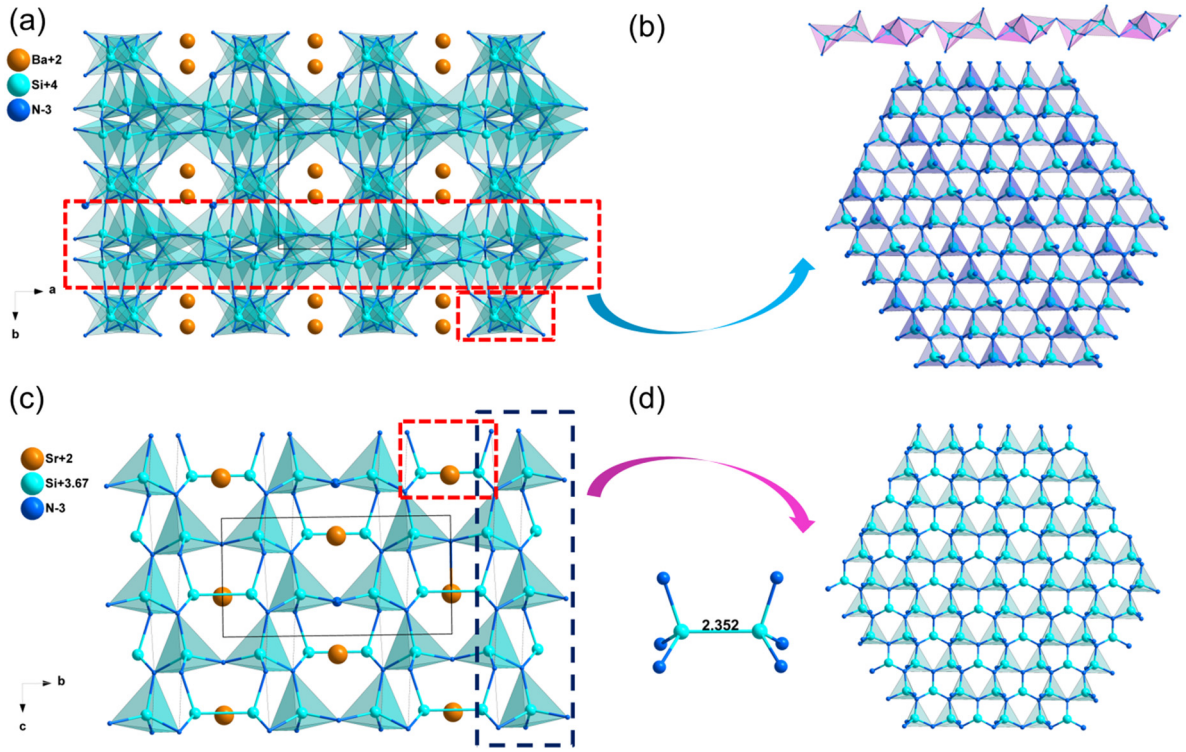

Fig. 6 Crystal structure of $BaSi_7N_{10}$ (a) and (b) and $SrSi_6N_8$ (c) and (d).

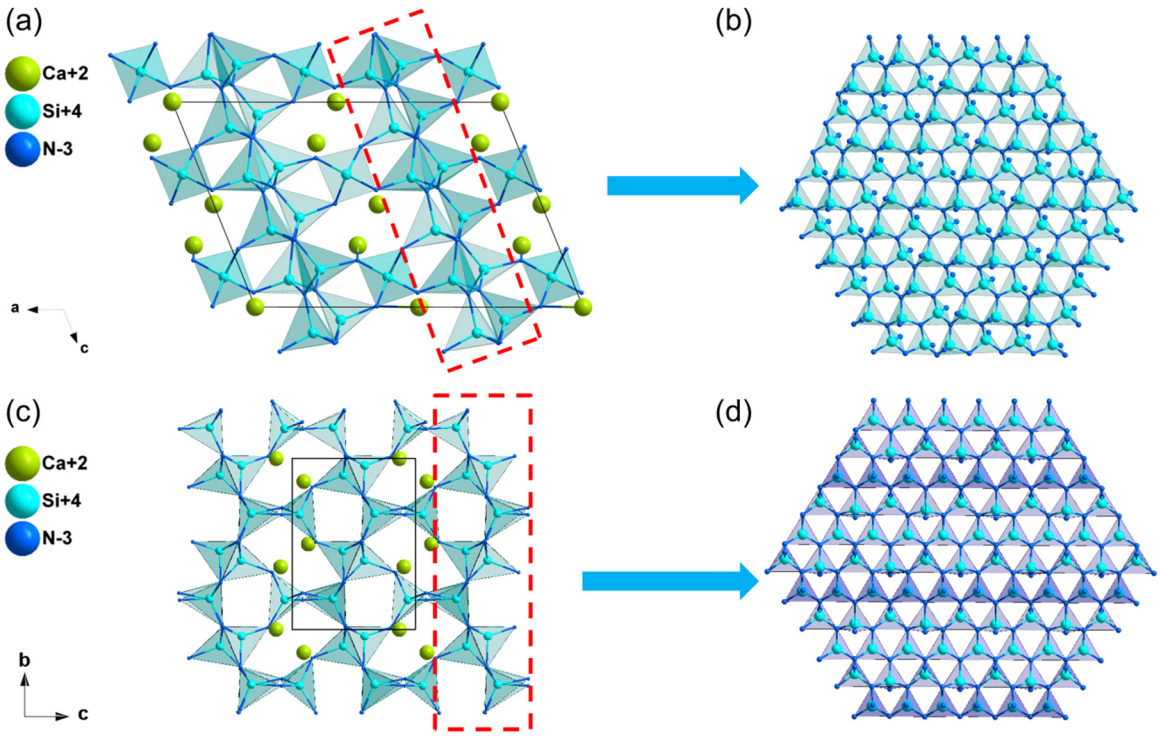

Fig. 7 Crystal structure of α-$Ca_2Si_5N_8$ (a) and (b) and β-$Ca_2Si_5N_8$ (c) and (d).

The calculated NLO coefficient is d_{14} = −0.28 pm V^{-1}. In addition, the birefringence of $Ca_3Al_2N_4$ is calculated to be 0.031 at 1064 nm. All these results were listed in Table 2.

$SrAlSi_4N_7$. The compound $SrAlSi_4N_7$ was first synthesized and studied in 2009 by Schnick *et al.*[76] $SrAlSi_4N_7$ crystallize in the polar space group $Pna2_1$, its structure featured layers

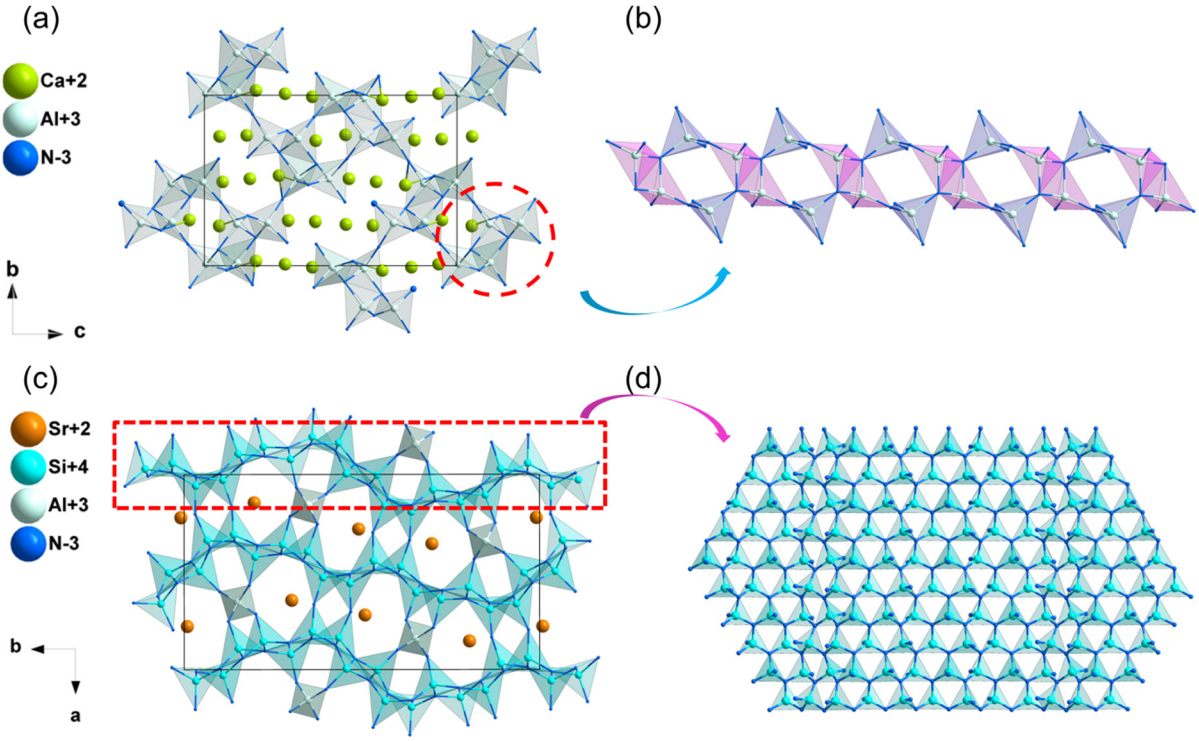

Fig. 8 Crystal structure of $Ca_3Al_2N_4$ (a) and (b) and $SrAlSi_4N_7$ (c) and (d).

consisting of [SiN_4] tetrahedra, which were linked inside the layers by sharing N atoms. And the layers are attached using [AlN_4] tetrahedra and N atoms as bridges to form the structural framework of $SrAlSi_4N_7$, where Sr^{2+} are added into the pores to balance the framework (Fig. 8c and d). The band gap calculated by HSE06 of $SrAlSi_4N_7$ is 4.04 eV, which is mainly dominated by the covalent Si–N bonds (Fig. S13b, ESI†). The calculated NLO coefficients are $d_{31} = -1.02$, $d_{32} = 1.43$, $d_{33} = -1.37$ pm V^{-1}, respectively. In addition, the birefringence of $SrAlSi_4N_7$ is calculated to be 0.028 at 1064 nm. All the above results were listed in Table 2.

$SrYSi_4N_7$. The synthesis and crystal structure of the compound $SrYSi_4N_7$ were reported in 2004.[77] $SrYSi_4N_7$ crystallizes in the hexagonal space group $P6_3mc$ and features C_2-type supertetrahedra.[78] The structural framework of $SrYSi_4N_7$ is assembled from layers constructed by [Si_4N_{11}] C_2-type supertetrahedra, which are connected by sharing the corners of the bottom [SiP_4] tetrahedra, and Sr^{2+} cations as well as [YN_6] octahedra are filled in the pores (Fig. 9a and b). The experimental band gap of $SrYSi_4N_7$ is 3.3–3.5 eV, while the calculated band gap is 4.21 eV (HSE06), which is mainly dominated by the covalent Y–N and Si–N bonds (Fig. S14c, ESI†). Moreover, the calculated NLO coefficients of $SrYSi_4N_7$ are $d_{31} = -1.25$ and $d_{33} = 6.45$ pm V^{-1}. The birefringence of $SrYSi_4N_7$ is calculated to be 0.012 at 1064 nm.

3.3. Other polyhedra-stacking type NLO nitrides

CrB_4O_5N. The synthesis and physical properties (including SHG performance) of CrB_4O_5N were investigated in 2021 by Huppertz *et al.*[79] CrB_4O_5N crystallizes in hexagonal space group $P6_3mc$. Interestingly, the structure of the chromium oxonitridoborate CrB_4O_5N is similar to that of the nitridosilicates $SrYSi_4N_7$. The structural framework of CrB_4O_5N could be regarded that the [Si_4N_{11}] C_2-type supertetrahedra were replaced by [$B_4O_9N_2$] C_2-type supertetrahedra(Fig. 9c and d). The calculated band gap of CrB_4O_5N is 1.96 eV (GGA), and the frontier orbitals (top of valence band and bottom of conduction band) of this compound are mainly occupied by the Cr-3d, indicating that the optical band gap is mainly decided on the Cr-3d orbital. Furthermore, the SHG response of CrB_4O_5N was about 0.8 times that of quartz.

$LaSi_3N_5$. $LaSi_3N_5$ was first synthesized and studied in 1995.[80] $LaSi_3N_5$ crystallizes in orthorhombic space group $P2_12_12_1$ and its crystal structure is depicted in Fig. 5b. In this structure, the [SiN_4] tetrahedra are interconnected by sharing N atoms and extend in space with La^{3+} added into the intervals to build the framework of $LaSi_3N_5$. The calculated results demonstrate that $LaSi_3N_5$ owns a wide band gap 4.53 eV (HSE06), which is mainly dominated by the covalent La–N bonds (Fig. S14d, ESI†). The NLO coefficient based on the DFT calculation for $LaSi_3N_5$ is $d_{14} = 2.50$ pm V^{-1}, and $LaSi_3N_5$ exhibits large birefringence with the calculated value of 0.037 at 1064 nm.

$Pb_2Si_5N_8$. The compound $Pb_2Si_5N_8$[81] crystallizes in orthorhombic space group $Pmn2_1$. $Pb_2Si_5N_8$ is isomorphic to $Sr_2Si_5N_8$ and $Ba_2Si_5N_8$, and features layers consisting of [SiN_4] tetrahedra. Notably, cations filled in the structural framework of $Pb_2Si_5N_8$ are different from that of $Sr_2Si_5N_8$ and $Ba_2Si_5N_8$ (Fig. S1b, ESI†), because Pb^{2+} contains activated lone pair

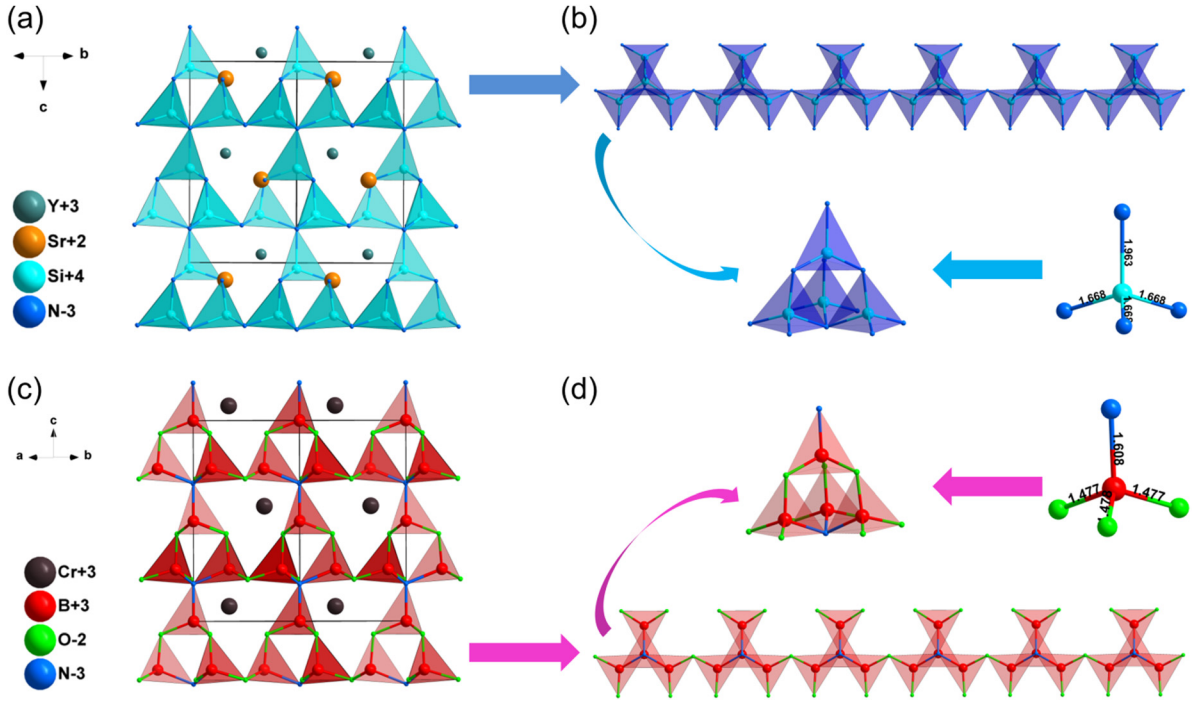

Fig. 9 Crystal structure of $SrYSi_4N_7$ (a) and (b) and CrB_4O_5N (c) and (d).

electrons, which could improve the SHG response for $Pb_2Si_5N_8$ compared with $Sr_2Si_5N_8$ and $Ba_2Si_5N_8$.[82–84] The calculated band gap of $Pb_2Si_5N_8$ is 3.17 eV (HSE06), which is mainly dominated by the covalent Si–N bonds (Fig. S14e, ESI†). Its calculated NLO coefficients are d_{31} = 6.46, d_{32} = −3.71, d_{33} = −11.84 pm V^{-1}, and the largest NLO tensor of $Pb_2Si_5N_8$ is larger than that of $Sr_2Si_5N_8$ (−1.22 pm V^{-1}) and $Ba_2Si_5N_8$ (1.73 pm V^{-1}). Furthermore, the birefringence of $Pb_2Si_5N_8$ is calculated to be 0.064 at 1064 nm.

4. Other NLO nitrides with featured structures

The structures of some nitrides exhibit low-dimensional special features, such as zero-dimensional (0D) molecules, one-dimensional (1D) chains and two-dimensional (2D) layers, and excellent properties may be realized in these nitrides with unique structures. Low-dimensional units, including $[BN_2]$ entities in $Ba_3B_2N_4$, $[Si_2N_6]$ dual-tetrahedra in $Ba_2Si_2N_6$, $[MoN_4]_n/[WN_4]_n$ chains in Na_3MoN_3/Na_3WN_3, $[SnN_3]_n$ layers in NaSnN and $[ZrN_6]_n$ layers in $ZnZrN_2$ are discussed in detail in this section. Results indicated that these NLO nitrides with low-dimensional structures exhibited large NLO coefficients and birefringence.

NaSnN

The synthesis and physical properties (including SHG performance) of compound NaSnN were first reported in 2005 by Clarke *et al*,[85] and the NLO properties were study by Lin *et al.* based on the first-principles calculations recently.[86] NaSnN crystallizes in hexagonal space group $P6_3mc$, and its structural framework built by infinite two-dimensional (2D) layers with Na^+ dispersed between layers, which are made up of $[SnN_3]$ triangular pyramids connecting each other through N atoms (Fig. 10a and b). In addition, the activated lone pair electrons in Sn^{2+} could enhance the second-order NLO response. The band gap by HSE06 of NaSnN is 1.70 eV, and the band gap between valence bands (VB) and conduction bands (CB) is dominated by the ionic Na–N coupling and covalent Sn–N hybridization. Moreover, the calculated NLO coefficients and birefringence are d_{13} = d_{23} = −2.7; d_{33} = 27 pm V^{-1} and 0.629 at 2.0 μm, respectively. All these results were listed in Table 3. The SHG-weighted density of NaSnN suggested that the $[SnN_3]_\infty$ backbone with the lone electron pairs effect leading to the large NLO coefficients.

Na_3MoN_3 and Na_3WN_3

Na_3MoN_3[87] and Na_3WN_3[88] are isostructural and crystallize in the monoclinic space group *Cc*. Their crystal structure featured one-dimensional (1D) infinite chains parallel to each other, constructed by vertex-sharing $[MoN_4]$ tetrahedra, and Na^+ are distributed between chains to balance the charge (Fig. 10c and d). Their computational band gaps are 2.1 and 2.41 eV (HSE06), respectively. The band gaps of Na_3MoN_3 and Na_3WN_3 between valence bands and conduction bands are dominated by the ionic Na–N bands and covalent Mo/W–N bands (Fig. S14f and S15a, ESI†). The calculated NLO coefficients are d_{11} = 11.98, d_{12} = −5.98, d_{13} = −6.04, d_{31} = −5.74, d_{32} = −3.42, d_{33} = −1.52 pm V^{-1} for Na_3MoN_3 and d_{11} = 11.98, d_{12} = −5.98, d_{13} = −6.04, d_{31} = −5.74, d_{32} = −3.42, d_{33} = −1.52 pm V^{-1} for Na_3WN_3 (Table 3), respectively. In addition, the calculated birefringence of Na_3MoN_3 and Na_3WN_3 is 0.119 and 0.079 at 1064 nm.

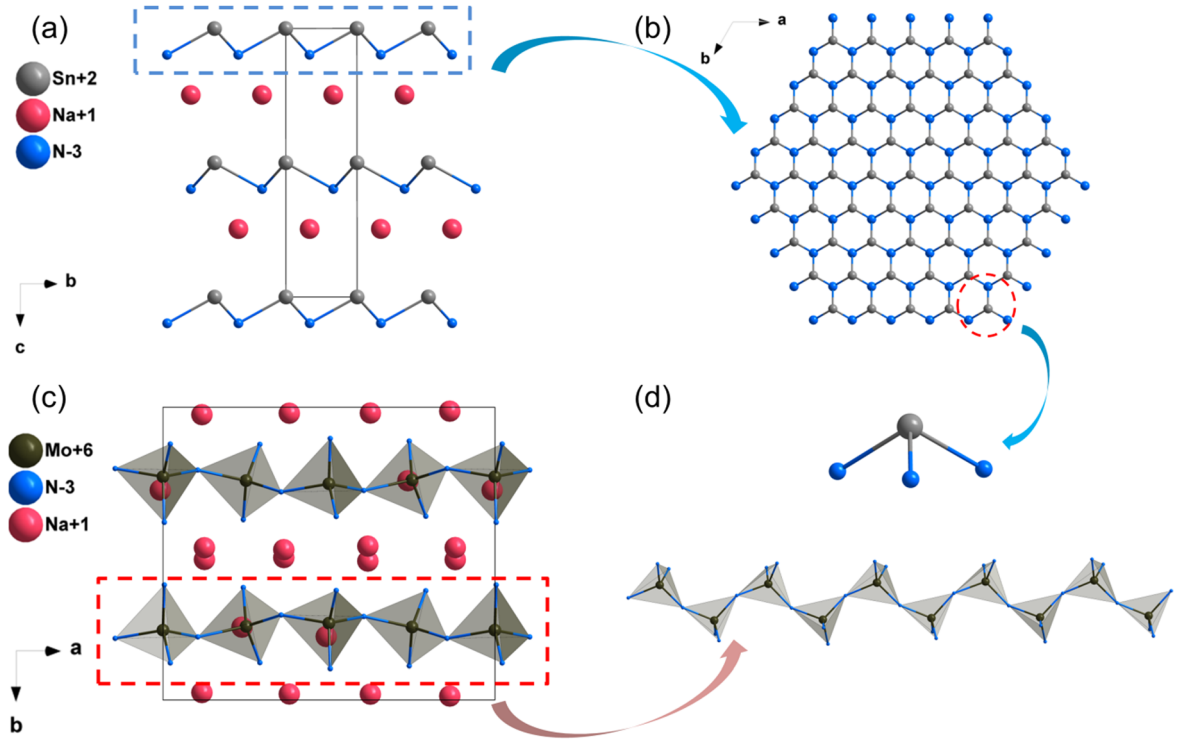

Fig. 10 Crystal structure of NaSnN (a), (b) and (d) Na_3MoN_4 (c) and (d).

Table 3 The NLO data of other nitrides with featured structures

Compounds	Space group	Band gap (eV)			NLO coefficients[a] (pm V^{-1})	Δn[a]	
		GGA[a]	HSE06[a]	Exp.[b]		At 1064 nm	At 2050 nm
NaSnN	$P6_3mc$	1.07	1.70	—	$d_{31} = d_{32} = -2.7$, $d_{33} = -27$ [b]	0.578[a]	0.629[b]
Na_3MoN_3	Cc	1.25	2.10	—	$d_{11} = 11.98$, $d_{12} = -5.98$, $d_{13} = -6.07$	0.119	0.086
				—	$d_{31} = -5.74$, $d_{32} = -3.42$, $d_{33} = -1.52$		
Na_3WN_3	Cc	1.51	2.41	—	$d_{11} = 6.21$, $d_{12} = -4.51$, $d_{13} = -3.04$	0.079	0.042
				—	$d_{31} = -0.65$, $d_{32} = -3.93$, $d_{33} = -1.49$		
$Ba_3B_2N_4$	$P2_12_12_1$	2.45	3.41	—	$d_{14} = d_{25} = d_{36} = -1.18$	0.189	0.182
$Ba_5Si_2N_6$	$P2_12_12_1$	1.45	2.32	—	$d_{14} = d_{25} = d_{36} = 1.88$	0.104	0.096
$ZrZnN_2$	$P3m1$	1.98[b]	3.11[b]	—	$d_{15} = 10.06$, $d_{33} = 2.15$[b]	0.276[b]	—
$MoSi_2N_4$	—	1.78[b]	2.24[b]	—	300 × SiO_2	—	—

[a] This work. [b] Other work from ref. 29, 83, 91–93.

$Ba_3B_2N_4$

The compound $Ba_3B_2N_4$[89] crystallizes in the orthorhombic space group $P2_12_12_1$. The structural framework of $Ba_3B_2N_4$ was made up of dumbbell-shaped [BN_2] entities with Ba^{2+} cations filled in the framework. Moreover, the dumbbell-shaped [BN_2] entities were almost parallel to the *b*-axis (Fig. 11a). According to calculated results, the HSE06 band gap of $Ba_3B_2N_4$ is 3.41 eV, and the band gap between valence bands and conduction bands is mainly dominated by the ionic Ba–N bands (Fig. S15b, ESI†). The calculated NLO coefficient is $d_{14} = -1.18$ pm V^{-1}. Furthermore, the birefringence of $Ba_3B_2N_4$ is calculated to be 0.189 at 1064 nm.

$Ba_5Si_2N_6$

The synthesis and crystal structure of compound $Ba_5Si_2N_6$[90] was reported in 1996 by DiSalvo *et al.* $Ba_5Si_2N_6$ crystallizes in the orthorhombic space group $P2_12_12_1$. In this structure, the isolated prism-sharing [Si_2N_6] dual-tetrahedra are the backbone of the structural framework of $Ba_5Si_2N_6$, and Ba^{2+} are dispersed in intervals between these tetrahedra to balance the charge (Fig. 11b). The calculated results implied that $Ba_5Si_2N_6$ owns a wide band gap of 2.32 eV (HSE06), and the band gap between valence bands and conduction bands is mainly dominated by the ionic Ba–N bands (Fig. S15c, ESI†). The calculated NLO coefficient is d_{14} = 1.88 pm V^{-1}. Moreover, the calculated birefringence of $Ba_5Si_2N_6$ is 0.104 at 1064 nm.

$ZrZnN_2$

$ZrZnN_2$ with high thermal conductivity has been studied as an IR NLO material by Yang *et al.* recently.[32] $ZrZnN_2$ crystalizes in the trigonal space group $P3m1$, in this structure, [ZrN_6] octahedra are connected by edge-sharing to build octahedral

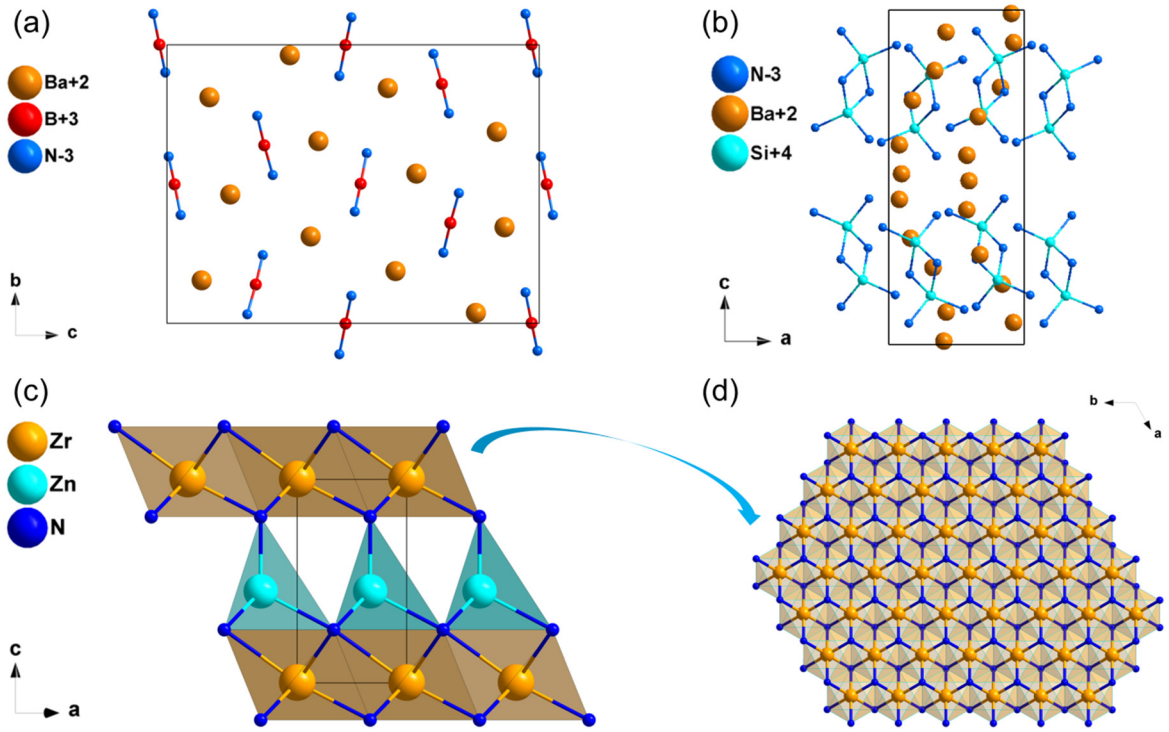

Fig. 11 Crystal structure of $Ba_3B_2N_4$ (a), $Ba_5Si_2N_6$ (b) and $ZrZnN_2$ (c) and (d).

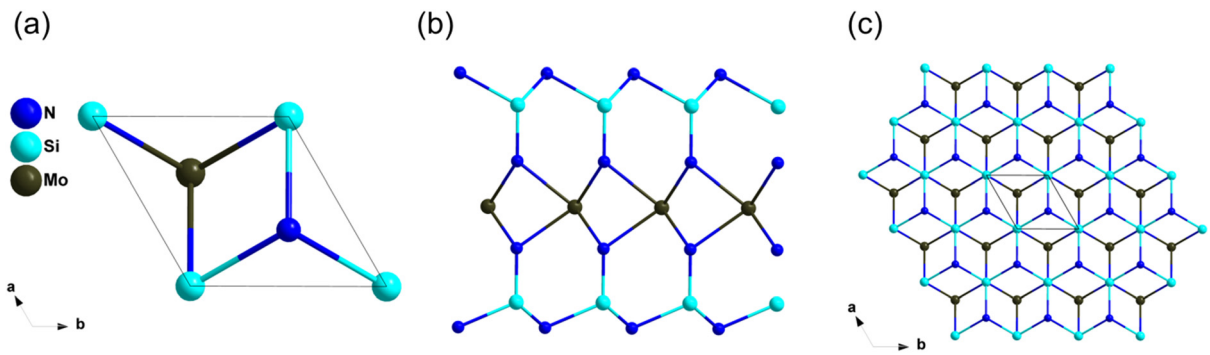

Fig. 12 The atomic structure of $MoSi_2N_4$.

layers, which are stacked in the *c* direction and connected by $[ZnN_4]$ tetrahedral (Fig. 11c and d). The band gap of $ZrZnN_2$ based on HSE06 is 3.11 eV, which is larger than that of $AgGaS_2$ (2.73 eV). Furthermore, $ZrZnN_2$ show balanced optical performance with the NLO coefficient of about 0.9 × AGS and the birefringence is of 0.276 at 1064 nm. Both $[ZrN_6]$ octahedra and $[ZnN_4]$ tetrahedra contributed to the NLO properties, including wide band gap and large NLO coefficients.

$MoSi_2N_4$

The growth of centimeter-scale monolayer films of $MoSi_2N_4$ was achieved in 2020 by Hong *et al*,[91] and the NLO properties were further studied by Lin *et al.* based on the first-principles calculations recently.[91,92] The atomic structure of $MoSi_2N_4$ was shown in Fig. 12, its structure features infinite two-dimensional (2D) N–Si–N–Mo–N–Si–N layers, which can be viewed as a MoN_2 layer sandwiched between two Si–N bilayers. The experimental optical band gap of monolayer $MoSi_2N_4$ film is 1.94 eV, and the band gap between valence bands (VB) and conduction bands (CB) is dominated by Mo–N bonds and Mo^{4+} nonbonding states. Furthermore, the SHG response of $MoSi_2N_4$ was about 300 times that of quartz, and the SHG response of $MoSi_2N_4$ mainly comes from the inner Mo–N bands of MoN_2 layers.

Conclusions and outlooks

In this review, we systematically summarize the potential and recent advancements in nitride-based NLO crystals, which include 45 nitrides. These crystals are classified into three categories based on their structural features: diamond-like type NLO nitrides, polyhedra-stacking type NLO nitrides, and other

NLO nitrides with unique structures. We consistently discuss their crystal structures, physical properties, and structure–property relationships. Our findings indicate that nitrides possess wide band gaps and transparency windows, ranging from the ultraviolet to the infrared region. Notably, several NLO nitrides exhibit outstanding NLO properties including $BeSiN_2$, $LiSi_2N_3$, LiSiON, $LiPO_2N$, Zn_3MoN_4, Zn_2NX (X = Cl, Br), $NaPN_2$, Pb_2Si5N_8, NaSnN, Na_3MoN_4 and $ZrZnN_2$. Furthermore, approximately 40% of these NLO nitrides contain elemental silicon, suggesting that Si-based nitrides warrant further exploration as NLO materials. However, the investigation of NLO nitrides is far from complete and faces numerous challenges, such as difficult synthesis conditions and unclear property influencing mechanisms. Consequently, the following aspects should be considered for the further application and development of NLO nitrides:

1. The development of new synthetic methods and advanced equipment technology is necessary to obtain more NLO nitrides with exceptional properties. Currently, most non-centrosymmetric nitrides are obtained using traditional solid-state synthesis technology under high temperature and pressure conditions. Advanced equipment technology is crucial for meeting these demanding conditions. Additionally, the ammonothermal method and salt-flux method may be effective ways to synthesize more NLO nitrides. Moreover, since high-performance NLO nitrides are predominantly available in powder or micron-sized crystal forms, further research on large-size crystal growth is needed.

2. A deeper understanding of the chemical bonding mechanisms between nitrides and pnictides is essential. Nitrogen and phosphorus belong to the same main group VA, while homocationic and homo-anionic bonds often form in pnictide crystal structures, they do not in nitrides. These homoatomic bonds significantly impact linear optical and NLO properties. Therefore, studying the bonding habits of nitrides and pnictides is crucial for designing excellent NLO materials.

3. Prioritizing the exploration of mixed-anion inorganic nitrides as NLO materials is recommended. Combining different anions into one structure can effectively enhance NLO properties. Consequently, halogens (Cl, Br, I) and phosphorus (P) can be introduced into nitrides to form $[MN_yX_{4-y}]$ (M = mental elements, X = Cl, Br, I, P) mixed anionic tetrahedra. These distorted tetrahedra possess large anisotropic polarizability and strong hyperpolarizability, which can improve the SHG response and birefringence.

4. Developing metal nitrides with triangular anionic groups MN_3 (M = Sb, Te, Sn) is suggested. MN_3 groups possess stereochemically active lone-pair electrons, and compounds containing these electrons exhibit significant SHG response and birefringence, as seen in NaSnN. Therefore, more in-depth investigations should be conducted to design NLO nitrides with triangular anionic groups.

Author contributions

Xin Zhao performed the theoretical calculation, data analysis, and paper writing; Chensheng Lin and Haotian Tian offered help in theoretical calculation; Chao Wang offered help in analyzing data; Ning Ye and Min Luo guided and revised the manuscript. All authors contributed to the general discussion.

Conflicts of interest

There are no conflicts to declare. The authors declare no competing financial interests.

Acknowledgements

This work was supported by the National Natural Science Foundation of China (22222510, 21975255 and 21921001), Natural Science Foundation of Fujian Province (2023J02026), the Foundation of Fujian Science & Technology Innovation Laboratory (2021ZR202), Youth Innovation Promotion Association CAS (2019303).

References

1 Z. H. Yang and S. L. Pan, Computationally assisted multi-stage design and prediction driving the discovery of deep-ultraviolet nonlinear optical materials, *Mater. Chem. Front.*, 2021, **5**, 3507–3523.
2 S. Cho and K. M. Ok, $LiRE(SO_4)_2$ (RE = Y, Gd, Eu): noncentrosymmetric chiral rare-earth sulfates with very large band gaps, *Mater. Chem. Front.*, 2022, **7**, 65–71.
3 L. Kang, F. Liang, X. X. Jiang, Z. S. Lin and C. T. Chen, First-Principles Design and Simulations Promote the Development of Nonlinear Optical Crystals, *Acc. Chem. Res.*, 2020, **53**, 209–217.
4 F. Xu, G. Zhang, M. Luo, G. Peng, Y. Chen, T. Yan and N. Ye, A Powder Method for The High-efficacy Evaluation of Electro-optic Crystals, *Natl. Sci. Rev.*, 2020, **8**, nwaa104.
5 X. M. Liu, L. Kang, P. F. Gong and Z. S. Lin, $LiZn(OH)CO_3$: A Deep-Ultraviolet Nonlinear Optical Hydroxycarbonate Designed from a Diamond-like Structure, *Angew. Chem., Int. Ed.*, 2021, **60**, 13574–13578.
6 C. Wu, C. B. Jiang, G. F. Wei, X. X. Jiang, Z. J. Wang, Z. S. Lin, Z. P. Huang, M. G. Humphrey and C. Zhang, Toward Large Second-Harmonic Generation and Deep-UV Transparency in Strongly Electropositive Transition Metal Sulfates, *J. Am. Chem. Soc.*, 2023, **145**, 3040–3046.
7 L. Wu, H. Fan, C. Lin and M. Luo, Compounds consisting of coplanar π-conjugated B_3O_6 – typed structures: An emerging source of ultraviolet nonlinear optical materials, *Chin. J. Struct. Chem.*, 2023, **42**, 100019.
8 F. J. Duarte, Tunable laser optics: Applications to optics and quantum optics, *Prog. Quantum Electron.*, 2013, **37**, 326–347.
9 C. T. Chen, G. L. Wang, X. Y. Wang and Z. Y. Xu, Deep-UV nonlinear optical crystal $KBe_2BO_3F_2$ – discovery, growth, optical properties and applications, *Appl. Phys. B: Lasers Opt.*, 2009, **97**, 9–25.

10 C. T. Chen, Y. C. Wu, A. D. Jiang, B. C. Wu, G. M. You, R. K. Li and S. J. Lin, New Nonlinear-optical crystal – LiB_3O_5, *J. Opt. Soc. Am. B*, 1989, **6**, 616–621.
11 D. N. Nikogosyan, *Nonlinear Optical Crystals: a Complete Survey*, Springer-Science and Business Media, New York, 2005.
12 W. L. Smith, KDP and ADP transmission in vacuum ultraviolet, *Appl. Optics*, 1977, **16**, 1798.
13 K. Kato, Parametric oscillation at 3.2 μm in KTP pumped at 1.064 μm, *IEEE J. Quantum Electron.*, 1991, **27**, 1137–1140.
14 A. O. Okorogu, S. B. Mirov, W. Lee, D. I. Crouthamel, N. Jenkins, A. Y. Dergachev, K. L. Vodopyanov and V. V. Badikov, Tunable middle infrared down-conversion in GaSe and $AgGaS_2$, *Opt. Commun.*, 1998, **155**, 307–312.
15 G. D. Boyd, F. G. Storz, J. H. McFee and H. M. Kasper, Linear and Nonlinear Optical Properties of Some Ternary Selenides, *IEEE J. Quantum Electron.*, 1972, **8**, 900–908.
16 G. D. Boyd, E. Buehler and F. G. Storz, Linear and Nonlinear Optical Properties of $ZnGeP_2$ and CdSe, *Appl. Phys. Lett.*, 1971, **18**, 301–304.
17 M. Mutailipu and S. L. Pan, Emergent Deep-Ultraviolet Nonlinear Optical Candidates, *Angew. Chem., Int. Ed.*, 2020, **59**, 20302–20317.
18 T. T. Tran, H. W. Yu, J. M. Rondinelli, K. R. Poeppelmeier and P. S. Halasyamani, Deep Ultraviolet Nonlinear Optical Materials, *Chem. Mater.*, 2016, **28**, 5238–5258.
19 W. Q. Huang, S. G. Zhao and J. H. Luo, Recent Development of Non-pi-Conjugated Deep Ultraviolet Nonlinear Optical Materials, *Chem. Mater.*, 2022, **34**, 5–28.
20 P. F. Gong, X. M. Liu, L. Kang and Z. S. Lin, Inorganic planar pi-conjugated groups in nonlinear optical crystals: review and outlook, *Inorg. Chem. Front.*, 2020, **7**, 839–852.
21 H. Su, Z. Yan, X. Hou and M. Zhang, Fluorooxoborates: A precious treasure of deep-ultraviolet nonlinear optical materials, *Chin. J. Struct. Chem.*, 2023, **42**, 100027.
22 B. Zhang and Z. Chen, Recent advances of inorganic phosphates with UV/DUV cutoff edge and large second harmonic response, *Chin. J. Struct. Chem.*, 2023, **42**, 100033.
23 L. Gao, J. Huang, S. Guo, Z. Yang and S. Pan, Structure-property survey and computer-assisted screening of mid-infrared nonlinear optical chalcohalides, *Coord. Chem. Rev.*, 2020, **421**, 213379.
24 P. Gong, F. Liang, L. Kang, X. Chen, J. Qin, Y. Wu and Z. Lin, Recent advances and future perspectives on infrared nonlinear optical metal halides, *Coord. Chem. Rev.*, 2019, **380**, 83–102.
25 H. D. Yang, M. Y. Ran, W. B. Wei, X. T. Wu, H. Lin and Q. L. Zhu, The Rise of Infrared Nonlinear Optical Pnictides: Advances and Outlooks, *Chem. – Asian J.*, 2021, **16**, 3299–3310.
26 J. Chen, X. Jiang, Q. Wu, Z. Lin, M. Luo and N. Ye, Pnictides: An emerging class of infrared nonlinear optical material candidates, *J. Alloys Compd.*, 2022, **901**, 163384.
27 W. H. Sun, C. J. Bartel, E. Arca, S. R. Bauers, B. Matthews, B. Orvananos, B. R. Chen, M. F. Toney, L. T. Schelhas, W. Tumas, J. Tate, A. Zakutayev, S. Lany, A. M. Holder and G. Ceder, A map of the inorganic ternary metal nitrides, *Nat. Mater.*, 2019, **18**, 732–739.
28 S. Yourdkhani, T. Korona and N. L. Hadipour, Structure and Energetics of Complexes of $B_{12}N_{12}$ with Hydrogen Halides—SAPT (DFT) and MP_2 Study, *J. Phys. Chem. A*, 2015, **119**, 6446–6467.
29 G. Seifert, P. W. Fowler, D. Mitchell, D. Porezag and T. Frauenheim, Boron-nitrogen analogues of the fullerenes: Electronic and structural properties, *Chem. Phys. Lett.*, 1997, **268**, 352–358.
30 X. Zhao, C. Lin, J. Chen, M. Luo, F. Xu, S. Yang, S. Shi, B. Li and N. Ye, Halonitrides Zn_2NX (X = Cl, Br): Novel Mid-Infrared Nonlinear Optical Materials, *Chem. Mater.*, 2021, **33**, 1462–1470.
31 J. Huang, S. Shu and G.-M. Cai, Screening Nitrides with High Debye Temperatures as Nonlinear Optical Materials, *J. Phys. Chem. C*, 2022, **126**, 7047–7053.
32 D. Chu, Y. Huang, C. Xie, E. Tikhonov, I. Kruglov, G. Li, S. Pan and Z. Yang, Unbiased Screening of Novel Infrared Nonlinear Optical Materials with High Thermal Conductivity: Long-neglected Nitrides and Popular Chalcogenides, *Angew. Chem., Int. Ed.*, 2023, **62**, e202300581.
33 J. B. Huang, C. W. Xie, L. Wei, Q. Bian, Z. H. Yang and S. Pan, Predicting Diamond-like Nitrides as Infrared Nonlinear Optical Materials with High Thermal Conductivity, *Chem. Mater.*, 2022, **34**, 10059–10067.
34 F. Liang, L. Kang, Z. Lin, Y. Wu and C. Chen, Analysis and prediction of mid-IR nonlinear optical metal sulfides with diamond-like structures, *Coord. Chem. Rev.*, 2017, **333**, 57–70.
35 A. Abudurusuli, J. B. Huang, P. Wang, Z. H. Yang, S. L. Pan and J. J. Li, $Li_4MgGe_2S_7$: The First Alkali and Alkaline-Earth Diamond-Like Infrared Nonlinear Optical Material with Exceptional Large Band Gap, *Angew. Chem., Int. Ed.*, 2021, **60**, 24131–24136.
36 M. Y. Li, Z. J. Ma, B. X. Li, X. T. Wu, H. Lin and Q. L. Zhu, $HgCuPS_4$: An Exceptional Infrared Nonlinear Optical Material with Defect Diamond-like Structure, *Chem. Mater.*, 2020, **32**, 4331–4339.
37 Y. Huang, K. Wu, J. N. Cheng, Y. Chu, Z. H. Yang and S. L. Pan, Li_2ZnGeS_4: a promising diamond-like infrared nonlinear optical material with high laser damage threshold and outstanding second-harmonic generation response, *Dalton Trans.*, 2019, **48**, 4484–4488.
38 T. T. Yu, S. P. Wang, X. Zhang, C. N. Li, J. Qiao, N. Jia, B. Han, S. Q. Xia and X. T. Tao, $MnSiP_2$: A New Mid-IR Ternary Phosphide with Strong SHG Effect and Ultrabroad Transparency Range, *Chem. Mater.*, 2019, **31**, 2010–2018.
39 J. Chen, C. Lin, D. Zhao, M. Luo, G. Peng, B. Li, S. Yang, Y. Sun and N. Ye, Anionic Aliovalent Substitution from Structure Models of ZnS: Novel Defect Diamond-like Halopnictide Infrared Nonlinear Optical Materials with Wide Band Gaps and Large SHG Effects, *Angew. Chem., Int. Ed.*, 2020, **59**, 23549–23553.
40 J. Chen, H. Chen, F. Xu, L. Cao, X. Jiang, S. Yang, Y. Sun, X. Zhao, C. Lin and N. Ye, $Mg_2In_3Si_2P_7$: A Quaternary

Diamond-like Phosphide Infrared Nonlinear Optical Material Derived from $ZnGeP_2$, *J. Am. Chem. Soc.*, 2021, **143**, 10309–10316.

41 R. A. Ferreyra, C. Zhu, A. Teke and H. Morkoç, in *Springer Handbook of Electronic and Photonic Materials*, ed. S. Kasap and P. Capper, Springer International Publishing, Cham, Switzerland, 2nd edn, 2017, Part D, 743–801.

42 V. I. Gavrilenko and R. Q. Wu, Linear and nonlinear optical properties of group-III nitrides, *Phys. Rev. B: Condens. Matter Mater. Phys.*, 2000, **61**, 2632–2642.

43 J. Chen, Z. H. Levine and J. W. Wilkins, Calculated second harmonic susceptibilities of BN, AlN, and GaN, *Appl. Phys. Lett.*, 1995, **66**, 1129–1131.

44 P. B. Perry and R. F. Rutz, The optical absorption edge of single crystal AlN prepared by a close spaced vapor process, *Appl. Phys. Lett.*, 1978, **33**, 319–321.

45 B. Monemar, Fundamental energy gap of GaN from photoluminescence excitation spectra, *Phys. Rev. B: Condens. Matter Mater. Phys.*, 1974, **10**, 676–681.

46 M. Orth and W. Schnick, On $LiSi_2N_3$ – Synthesis and crystal structure refinement, *Z. Anorg. Allg. Chem.*, 1999, **625**, 1426–1428.

47 J. Hausler, R. Niklaus, J. Minar and W. Schnick, Ammonothermal Synthesis and Optical Properties of Ternary Nitride Semiconductors Mg-IV-N_2, Mn-IV-N_2 and Li-IV_2-N_3 (IV = Si, Ge), *Chem. – Eur. J.*, 2018, **24**, 1686–1693.

48 Y. Q. Li, N. Hirosaki, R. J. Xie, T. Takeka and M. Mitomo, Crystal, electronic structures and photoluminescence properties of rare-earth doped $LiSi_2N_3$, *J. Solid State Chem.*, 2009, **182**, 301–311.

49 P. Eckerlin, Zur Kenntnis des Systems Be_3N_2–Si_3N_4·4. Die Kristallstruktur von $BeSiN_2$, *Z. Anorg. Allg. Chem.*, 1967, **353**, 225–236.

50 J. David, Y. Laurent and J. Lang, Structure of $MgSiN_2$ and Mg GeN_2, *Bull. Mineral.*, 1970, **93**, 153–159.

51 J. Hausler, S. Schimmel, P. Wellmann and W. Schnick, Ammonothermal Synthesis of Earth-Abundant Nitride Semiconductors $ZnSiN_2$ and $ZnGeN_2$ and Dissolution Monitoring by In Situ X-ray Imaging, *Chem. – Eur. J.*, 2017, **23**, 12275–12282.

52 E. Arca, S. Lany, J. D. Perkins, C. Bartel, J. Mangum, W. H. Sun, A. Holder, G. Ceder, B. Gorman, G. Teeter, W. Tumas and A. Zakutayev, Redox-Mediated Stabilization in Zinc Molybdenum Nitrides, *J. Am. Chem. Soc.*, 2018, **140**, 4293–4301.

53 V. SchultzCoulon and W. Schnick, Mg_2PN_3 and Ca_2PN_3 – Phosphorus(v) nitrides with infinite chains of corner sharing PN4 tetrahedra, *Z. Anorg. Allg. Chem.*, 1997, **623**, 69–74.

54 S. J. Sedlmaier, M. Eberspacher and W. Schnick, High-Pressure Synthesis, Crystal Structure, and Characterization of Zn_2PN_3 – A New catena-Polynitridophosphate, *Z. Anorg. Allg. Chem.*, 2011, **637**, 362–367.

55 K. N. Heinselman, S. Lany, J. D. Perkins, K. R. Talley and A. Zakutayev, Thin Film Synthesis of Semiconductors in the Mg–Sb–N Materials System, *Chem. Mater.*, 2019, **31**, 8717–8724.

56 M. Mallmann, C. Maak, R. Niklaus and W. Schnick, Ammonothermal Synthesis, Optical Properties, and DFT Calculations of Mg_2PN_3 and Zn_2PN_3, *Chem. – Eur. J.*, 2018, **24**, 13963–13970.

57 R. Marchand, P. Lharidon and Y. Laurent, Crystallochemical Study of $LiPN_2$ – A Structure Derived from Cristobalite, *J. Solid State Chem.*, 1982, **43**, 126–130.

58 F. J. Pucher, F. Hummel and W. Schnick, $CuPN_2$: Synthesis, Crystal Structure, and Electronic Properties, *Eur. J. Inorg. Chem.*, 2015, 1886–1891.

59 Y. Laurent, J. Guyader and G. Roult, Time-of-flight neutron diffraction study of α-LiSiON, *Acta Crystallogr., Sect. B: Struct. Sci.*, 1981, **37**, 911–913.

60 K. Senevirathne, C. S. Day, M. D. Gross, A. Lachgar and N. A. W. Holzwarth, A new crystalline LiPON electrolyte: Synthesis, properties, and electronic structure, *Solid State Ion.*, 2013, **233**, 95–101.

61 H. Jacobs and H. Mengis, Preparation and Crystal-Structure of a Sodium SiliconI-nitride, $NaSi_2N_3$, *Eur. J. Solid State Inorg. Chem.*, 1993, **30**, 45–53.

62 J. Guyader, P. L. Haridon, Y. Laurent, R. Jacquet and G. Roult, A new nitrogen tetrahedron NaN_4: Preparation and structure of $NaGe_2N_3$, *J. Solid State Chem.*, 1984, **54**, 251–255.

63 K. Landskron, S. Schmid and W. Schnick, High-pressure synthesis, crystal structure, and properties of $NaPN_2$, *Z. Anorg. Allg. Chem.*, 2001, **627**, 2469–2472.

64 Z. Li, A. Tudi, P. Ren, Y. Yang, T. Iitaka, T. Tohyama, Z. Yang, S. Pan and H. Su, $NaPN_2$: Deep-ultraviolet nonlinear optical material with unprecedented strong second-harmonic generation coefficient, *Phys. Rev. Mater.*, 2019, **3**, 025201.

65 Y. Laurent, M. Maunaye, J. Guyader and J. Lang, Étude structurale de $CaGeN_2$ et $Ca_{1-x}GeN_2$, *Bull. Mineral.*, 1971, 347–352.

66 F. J. Pucher, A. Marchuk, P. J. Schmidt, D. Wiechert and W. Schnick, Luminescent Nitridophosphates CaP_2N_4:Eu^{2+}, SrP_2N_4:Eu^{2+}, BaP_2N_4:Eu^{2+}, and $BaSr_2P_6N_{12}$:Eu^{2+}, *Chem. – Eur. J.*, 2015, **21**, 6443–6448.

67 F. W. Karau, L. Seyfarth, O. Oeckler, J. Senker, K. Landskron and W. Schnick, The stuffed framework structure of SrP_2N_4: Challenges to synthesis and crystal structure determination, *Chem. – Eur. J.*, 2007, **13**, 6841–6852.

68 T. Schlieper, W. Milius and W. Schnick, Nitridosilicates 2. High-temperature Syntheses and Crystal-structure of $Sr_2Si_5N_8$ and $Ba_2Si_5N_8$, *Z. Anorg. Allg. Chem.*, 1995, **621**, 1380–1384.

69 G. Pilet, H. A. Hoppe, W. Schnick and S. Esmaeilzadeh, Crystal structure and mechanical properties of $SrSi_7N_{10}$, *Solid-State Sci.*, 2005, **7**, 391–396.

70 H. Huppertz and W. Schnick, Edge-sharing SiN_4 tetrahedra in the highly condensed nitridosilicate $BaSi_7N_{10}$, *Chem. – Eur. J.*, 1997, **3**, 249–252.

71 F. Stadler, O. Oeckler, J. Senker, H. A. Hoppe, P. Kroll and W. Schnick, $SrSi_6N_8$ – A reduced nitridosilicate with a Si–Si bond, *Angew. Chem., Int. Ed.*, 2005, **44**, 567–570.

72 T. Schlieper and W. Schnick, Nitridosilicates 1. High-temperature Syntheses and Crystal-structure of $Ca_2Si_5N_8$, *Z. Anorg. Allg. Chem.*, 1995, **621**, 1037–1041.

73 P. Bielec, O. Janka, T. Block, R. Pottgen and W. Schnick, $Fe_2Si_5N_8$: Access to Open-Shell Transition-Metal Nitridosilicates, *Angew. Chem., Int. Ed.*, 2018, **57**, 2409–2412.

74 P. Bielec and W. Schnick, Increased Synthetic Control-Gaining Access to Predicted $Mg_2Si_5N_8$ and β-$Ca_2Si_5N_8$, *Angew. Chem., Int. Ed.*, 2017, **56**, 4810–4813.

75 M. Ludwig, J. Jager, R. Niewa and R. Kniep, Crystal structures of two polymorphs of $Ca_3Al_2N_4$, *Inorg. Chem.*, 2000, **39**, 5909–5911.

76 C. Hecht, F. Stadler, P. J. Schmidt, J. S. A. der Guenne, V. Baumann and W. Schnick, $SrAlSi_4N_7$:Eu^{2+} – A Nitridoalumosilicate Phosphor for Warm White Light (pc)LEDs with Edge-Sharing Tetrahedra, *Chem. Mater.*, 2009, **21**, 1595–1601.

77 Y. Q. Li, C. M. Fang, G. de With and H. T. Hintzen, Preparation, structure and photoluminescence properties of Eu^{2+} and Ce^{3+}-doped $SrYSi_4N_7$, *J. Solid State Chem.*, 2004, **177**, 4687–4694.

78 Z. Qian, Q. Bian, H. P. Wu, H. W. Yu, Z. S. Lin, Z. G. Hu, J. Y. Wang and Y. C. Wu, β-$BaGa_4Se_7$: a promising IR nonlinear optical crystal designed by predictable structural rearrangement, *J. Mater. Chem. C*, 2021, **10**, 96–101.

79 B. Fuchs, D. Johrendt, L. Bayarjargal and H. Huppertz, The First High-Pressure Chromium Oxonitridoborate CrB_4O_6N-an Unexpected Link to Nitridosilicate-Chemistry, *Angew. Chem., Int. Ed.*, 2021, **60**, 21801–21806.

80 M. Woike and W. Jeitschko, Preparation and Crystal-structure of the Nitridosilicates $Ln_3Si_6N_{11}$(Ln = La, Ce, Pr, Nd, Sm) and $LnSi_3N_5$ (Ln = Ce, Pr, Nd), *Inorg. Chem.*, 1995, **34**, 5105–5108.

81 P. Bielec, R. Nelson, R. P. Stoffel, L. Eisenburger, D. Gunther, A. K. Henss, J. P. Wright, O. Oeckler, R. Dronskowski and W. Schnick, Cationic Pb_2 Dumbbells Stabilized in the Highly Covalent Lead Nitridosilicate $Pb_2Si_5N_8$, *Angew. Chem., Int. Ed.*, 2019, **58**, 1432–1436.

82 W. F. Chen, B. W. Liu, S. M. Pei, X. M. Jiang and G. C. Guo, $K_2PbX\ Ga_7S_{12}$ (X = Cl, Br, I): The First Lead-Containing Cationic Moieties with Ultrahigh Second-Harmonic Generation and Band Gaps Exceeding the Criterion of 2.33 eV, *Adv. Sci.*, 2023, **10**, 2207630.

83 X. L. Chen, Q. Jing and K. M. Ok, $Pb_{18}O_8Cl_{15}I_5$: A Polar Lead Mixed Oxyhalide with Unprecedented Architecture and Excellent Infrared Nonlinear Optical Properties, *Angew. Chem., Int. Ed.*, 2020, **59**, 20323–20327.

84 M. Abudoureheman, S. J. Han, B. H. Lei, Z. H. Yang, X. F. Long and S. L. Pan, $KPb_2(PO_3)_5$: a novel nonlinear optical lead polyphosphate with a short deep-UV cutoff edge, *J. Mater. Chem. C*, 2016, **4**, 10630–10637.

85 N. S. P. Watney, Z. A. Gal, M. D. S. Webster and S. J. Clarke, The first ternary tin(II) nitride: NaSnN, *Chem. Commun.*, 2005, 4190–4192.

86 S. Zhang, L. Kang and Z. Lin, Nonlinear optical ASnX (A = Na, H; X = N, P) nanosheets with divalent tin lone electron pair effect by first-principles design, *Nanoscale*, 2020, **12**, 14895–14902.

87 D. Ostermann, U. Zachwieja and H. Jacobs, Sodium nitride metallates, Na_3MN_3, of molybd/in (VI) and Tungsten(VI) with $[CrO_20_{2/2}]$-isosteric $[MoN_2N_{2/2}]_3$ chains, *J. Alloys Compd.*, 1992, **190**, 137–140.

88 H. Jacobs and R. Niewa, Synthesis and crystal-structure- of a Sodium Nitrido tungstate(VI), Na_3WN_3, *Eur. J. Solid State Inorg. Chem.*, 1994, **31**, 105–113.

89 O. Reckeweg, F. J. DiSalvo and M. Somer, Orthorhombic $Ba_3(BN_2)_2$: a new structure type for an alkaline earth metal nitrido borate, *J. Alloys Compd.*, 2003, **361**, 102–107.

90 H. Yamane and F. J. DiSalvo, Preparation and crystal structure of a new barium silicon nitride, $Ba_5Si_2N_6$, *J. Alloys Compd.*, 1996, **240**, 33–36.

91 Y. L. Hong, Z. B. Liu, L. Wang, T. Y. Zhou, W. Ma, C. Xu, S. Feng, L. Chen, M. L. Chen, D. M. Sun, X. Q. Chen, H. M. Cheng and W. C. Ren, Chemical vapor deposition of layered two-dimensional $MoSi_2N_4$ materials, *Science*, 2020, **369**, 670–674.

92 L. Kang and Z. S. Lin, Second harmonic generation of $MoSi_2N_4$ – type layers, *Phys. Rev. B*, 2021, **103**, 195404.

93 J. S. Yang, L. N. Zhao, S. Q. Li, H. S. Liu, L. Wang, M. D. Chen, J. F. Gao and J. J. Zhao, Accurate electronic properties and non-linear optical response of two-dimensional MA_2Z_4, *Nanoscale*, 2021, **13**, 5479–5488.